η CARINAE ACROSS THE 2003.5 MINIMUM: SPECTROSCOPIC EVIDENCE FOR MASSIVE BINARY INTERACTIONS

K. E. Nielsen,[1,2] M. F. Corcoran,[3,4] T. R. Gull,[2] D. J. Hillier,[5] K. Hamaguchi,[3,4] S. Ivarsson,[1] and D. J. Lindler[2,6]

ABSTRACT

We have analyzed high spatial, moderate spectral resolution observations of η Carinae (η Car) obtained with the STIS from 1998.0 to 2004.3. The data were obtained at discrete times covering an entire 2024 day spectroscopic cycle, with focus on the X-ray/ionization low state that began in 2003 June. The spectra show prominent P Cygni lines in H I, Fe II, and He I, which are complicated by blends and contamination by nebular emission and absorption. All lines show phase- and species-dependent variations in emission and absorption. For most of the cycle the He I emission is blueshifted relative to the H I and Fe II P Cygni emission lines, which are centered at approximately system velocity. The blueshifted He I absorption components vary in intensity and velocity throughout the 2024 day period. We construct radial velocity curves for the absorption component of the He I and H I lines. The He I absorption shows significant radial velocity variations throughout the cycle, with a rapid change of over 200 km s^{-1} near the 2003.5 event. The H I velocity curve is similar to that of the He I absorption, although offset in phase and reduced in amplitude. We interpret the complex line profile variations in He I, H I, and Fe II to be a consequence of the dynamic interaction of the dense wind of η Car A with the less dense, faster wind plus the radiation field of a hot companion star, η Car B. We use the variations seen in He I and the other P Cygni lines to constrain the geometry of the orbit and the character of η Car B.

Subject headings: binaries: spectroscopic — stars: individual (η Carinae) — stars: winds, outflows

1. INTRODUCTION

Eta Carinae (η Car) is a superluminous, unstable object that underwent a rapid brightening in the 1840s, accompanied by ejection of a substantial amount of material. These ejecta now form a structured, bipolar nebula, the Homunculus, which makes direct observations of the star difficult. Hence, the nature of η Car has long been debated. Most observations up through the mid-1990s could be interpreted as arising from either a single star or binary system (Davidson 1997). More recent evidence favors the binary star interpretation. Indirect signatures of the companion star are periodic events first discovered as intensity variations in He I λ10830 (Damineli 1996 and references therein) with a 5.5 yr periodicity. The excitation events are accompanied by eclipse-like minima observed with *UBV* and *BVR* photometry (van Genderen et al. 2003), in near-infrared *JHKL* photometry (Whitelock et al. 2004), and in X-ray brightness (Ishibashi et al. 1999; Corcoran 2005). The X-ray light curve as measured with the *Rossi X-Ray Timing Explorer* (*RXTE*) is characterized by a gradual increase in brightness just before a rapid decline to a low state that lasts ∼70 days. *RXTE* observations of two such cycles fixed the orbital period to 2024 ± 2 days (5.54 yr), which is in agreement with the period derived from the infrared observations and from the He I λ10830 variability. Emission from the Weigelt blobs (Weigelt & Ebersberger 1986) located within 0.3″ of η Car also shows low-excitation intervals tracing the spectroscopic period, with emission from highly ionized species such as [Ar III] and [Fe IV] disappearing during the short spectroscopic minimum. Verner et al. (2005) attributed

this variation to the visible presence of an additional source of flux, possibly an O or Of/WN7 star with $T_{\rm eff} \sim 37,000$ K, during the time outside of the minima.

The X-ray variations, as seen by *RXTE*, *Chandra*, and *XMM-Newton*, have been modeled as a collision between a massive wind of the primary star (η Car A) and a less dense wind of the hot companion (η Car B) in a highly elliptical orbit (Ishibashi et al. 1999; Corcoran et al. 2001; Hamaguchi et al. 2007). Additional evidence for the presence of a binary component is the detection of He II λ4686, which appeared in ground-based spectra of η Car (Steiner & Damineli 2004; Stahl et al. 2005) shortly before the minimum but disappeared at the onset of the minimum. Gull (2005) and Martin et al. (2006) confirmed the presence of He II λ4686 with high angular resolution *Hubble Space Telescope* (*HST*) Space Telescope Imaging Spectrograph (STIS) spectra, and Martin et al. (2006) proposed that the He II λ4686 emission is formed in the interface between the stellar winds or possibly arises from photoionization by the companion star.

The multiwavelength variations observed in η Car have been interpreted as arising from the interaction of the winds of η Car A and η Car B or the impact of the radiation from the hot η Car B on the circumstellar material. Recently, Iping et al. (2005) reported evidence of the companion through detection with the *Far Ultraviolet Spectroscopic Explorer* (*FUSE*) of a source of far-UV radiation that disappeared just before the beginning of the 2003.5 event and reappeared by 2004 March.

Binary system models have been discussed by Damineli et al. (1997), Ishibashi et al. (1999), Corcoran et al. (2001), Falceta-Gonçalves et al. (2005), and Soker (2005), among others. In these models the far-UV flux from a hot companion alters the ionization state of η Car A's wind, while X-rays are produced in a bow shock due to the collision of the dense wind of η Car A with the lower density, higher velocity wind of η Car B. In most of the colliding wind binary models, the low state in observed X-ray intensity, the brightness in He I λ10830 and in the visible band, IR, and radio fluxes, occurs when η Car B, along with the wind-wind collision

[1] Catholic University of America, Washington, DC 20064.
[2] NASA Goddard Space Flight Center, Astrophysics Science Division, Code 667, Greenbelt, MD 20771; nielsen@milkyway.gsfc.nasa.gov.
[3] NASA Goddard Space Flight Center, CRESST, Astrophysics Science Division, Code 662, Greenbelt, MD 20771.
[4] Universities Space Research Association, Columbia, MD 21044.
[5] Department of Physics and Astronomy, University of Pittsburgh, Pittsburgh, PA 15260.
[6] Sigma Space Corporation, Lanham, MD 20706.

region, moves behind η Car A and is occulted by its dense wind. Other interpretations are that the reduction in X-ray flux is primarily due to mass transfer between the stars for a brief period near periastron passage (Soker 2005) or that the X-ray flux is reduced by a dense accumulation of wind material trailing η Car B after periastron passage (Falceta-Gonçalves et al. 2005). In the Falceta-Gonçalves et al. (2005) model, the companion star is positioned between the observer and the primary star during the periastron passage. This orientation is difficult to reconcile with the radiation cutoff observed toward the Weigelt blobs during the minimum. The Weigelt blobs are located on the same side of η Car as the observer, based on proper motions and observed blueshifted emission (Davidson & Humphreys 1997; Zethson 2001; Nielsen et al. 2007). The Falceta-Gonçalves et al. (2005) orientation is also difficult to reconcile with *HST* Advanced Camera for Surveys (ACS) imagery (Smith et al. 2004).

The η Car binary system bears striking similarities to the canonical long-period colliding wind binary, WR 140. WR 140 is a massive system (total system mass $\sim 70\,M_\odot$) composed of a WC7 +O4−5 pair in a 7.9 yr, highly eccentric orbit (Marchenko et al. 2003). The strong wind from the WC7 star dominates the emission from the system, although the O4−5 star is the more massive component and dominates the total luminosity of the system. WR 140 is an X-ray variable, with an X-ray light curve that rapidly climbs to a maximum of $\sim 5 \times 10^{33}$ ergs s^{-1} in the 0.5–10 keV band, followed by a rapid decline to minimum near periastron passage (Pollock et al. 2005). Like η Car, WR 140 shows infrared (Williams et al. 1990) and radio (White & Becker 1995) variability correlated with the orbital period. Like η Car, the infrared brightness of WR 140 peaks near periastron passage, while the radio flux drops precipitously at that time. Unlike η Car, in WR 140 both stellar components can be directly observed; and unlike η Car, WR 140 is not shrouded by thick circumstellar ejecta.

As part of an *HST* Treasury project,[7] η Car was observed with *HST* STIS throughout the 2024 day (5.54 yr) cycle including the spectroscopic low state that began on 2003 June 29. The STIS spectra provide the highest spatial resolution spectrometry of the star ever obtained and thus offer the best data set to decouple stellar changes from changes in the circumstellar nebula. STIS's extended wavelength coverage into the ultraviolet probed for direct evidence of the companion star in the form of excess continuum and potential wind lines characteristic of a hot star. The optical wind lines in the stellar spectrum are excellent diagnostics of the companion's influence on η Car A's wind. Of particular importance are the P Cygni lines from excited levels in neutral helium. The population of the excited helium energy states requires high-energy photons and is dependent on the radiation from the companion star. Verner et al. (2005) found that radiation from η Car B is necessary to produce nebular He I emission lines observed in the spectra of the Weigelt blobs.

This paper describes the characteristics of the He I lines in the STIS spectra throughout the orbit and compares their behavior to lines in H I, Fe II, and [N II]. Since these lines are formed under different physical conditions in the η Car system, they sample the response of the system to the interactions with the companion. We derive a velocity curve based on the He I absorption and show that it is similar to the expected photospheric radial velocity curve for a star in a highly eccentric orbit. The spectral line analysis is used to constrain the system parameters and indicates that the He I absorption column samples a spatially complex region that changes continuously throughout the spectroscopic period due to dynamical and radiative interactions between the two stars in the η Car system.

2. OBSERVATIONS

Spectroscopic observations were conducted with the *HST* STIS beginning 1998 January 1, just after the X-ray drop, as seen by *RXTE* (Corcoran 2005), and continuing at selected intervals through 2004 March 6. The data set covers more than one full spectroscopic period (5.54 yr), with a focus on the 2003.5 event as a part of the η Car *HST* Treasury project. The relatively short time span of the observation (6.2 yr), compared to the spectroscopic period, restricts comparisons between long-term trends and cyclic variations. To better understand the long-term trends, we need to have high spectral and spatial resolution spectra with good temporal sampling across the next event, occurring in early 2009. All observations utilized the $52'' \times 0.1''$ long aperture in combination with the G430M or G750M gratings, yielding a spectral resolving power of $R \sim 6000$–8000 and a signal-to-noise ratio of 50–100 per spectral resolution element. As observations were desired at critical phases of the period, spacecraft solar power restrictions determined the slit position angle. Hence, the observations were done with a range of position angles. When possible, observations were scheduled with slit orientation at position angle of $-28°$ or $152°$ to include the spatially resolved Weigelt B and D blobs within the long aperture. With superb cooperation with the *HST* schedulers, this was accomplished several times throughout the 6.2 yr observational interval.

The advantage of *HST* STIS over ground-based instruments is the high angular resolution, which permits exclusion of the bright nebular contributions of scattered starlight and nebular emission lines. While an ideal extraction of 2 pixels ($0.101''$) would be desirable, reduction issues due to small tilts of the dispersed spectrum with respect to the CCD rows can lead to an artificially induced modulation of the point-source spectrum. A tailored data reduction using interpolation was accomplished with half-pixel sampling by Davidson, Ishibashi, and Martin[8] minimizing the modulation. We determined that a six half-pixel extraction ($0.152''$) of the online reduced data provided an accurate measure of the stellar spectra while minimizing the nebular contamination. The $0.152''$ extraction covers a region corresponding to ~ 350 AU at the distance of η Car, i.e., much larger than the major axis of the binary orbit (30 AU). The six half-pixel extraction excludes most of the radiation from the Weigelt blobs located 230–575 AU from η Car, characterized by narrow-line emission. However, even with the $0.152''$ extraction the wind lines are slightly influenced by some of the strong nebular emission features. The observed spectra used in this paper, with corresponding orbital phase,[9] are summarized in Table 1. The complete *HST* STIS spectra for all phases are available online.[10]

3. SPECTRAL ANALYSIS

The spectrum of η Car contains a wealth of information. The spectrum is dominated by wind lines from η Car A, in particular the H I Balmer and Paschen series and numerous lines from the singly ionized iron group elements. A detailed discussion of the optical spectrum and its formation is given by Hillier et al. (2001). The UV wind spectrum is described in Hillier et al. (2001, 2006), where the general characteristics are discussed including the absence of wind lines from η Car B. We concentrate on the orbital phase dependence of four species whose spectra dominate the optical wavelength region: H I (ionization potential [IP] 13.6 eV), He I (IP 24.6 eV), Fe II (Fe II IP 16.2 eV with Fe III IP 30.7 eV),

---

[7] See http://archive.stsci.edu/prepds/etacar/.

[8] See http://etacar.umn.edu.

[9] All observations in this paper are referenced to the beginning of the *RXTE* low state 1997.9604: JD 2,450,799.792+2024 × ϕ (Corcoran 2005).

[10] See http://archive.stsci.edu/prepds/etacar/ or http://etacar.umn.edu.

TABLE 1
DATA USED IN THIS ANALYSIS

Proposal ID	Observation Date	JD (+2,450,000)	Orbital Phase, ϕ^a	Position Angle (deg)
7302[b]................................	1998 Jan 1	0814	0.007	−100
	1998 Mar 19	0891	0.045	−28
8036[c]................................	1998 Nov 25	1142	0.169	133
	1999 Feb 21	1231	0.213	−28
8327[b]................................	2000 Mar 13	1616	0.403	−41
8483[c]................................	2000 Mar 20	1623	0.407	−28
8619[b]................................	2001 Apr 17	2017	0.601	22
9083[b]................................	2001 Oct 1	2183	0.683	165
8619[b]................................	2001 Nov 27	2240	0.712	−131
9083[b]................................	2002 Jan 19–20	2294	0.738	−82
9337[b]................................	2002 Jul 4	2460	0.820	69
9420[b]................................	2002 Dec 16	2664	0.921	−115
	2003 Feb 12–13	2683	0.930	−57
	2003 Mar 29	2727	0.952	−28
	2003 May 5	2764	0.970	27
	2003 May 17	2776	0.976	38
	2003 Jun 1	2792	0.984	62
	2003 Jun 22	2813	0.995	70
9973[b]................................	2003 Jul 5	2825	1.001	69
	2003 Jul 29	2851	1.013	105
	2003 Sep 22	2904	1.040	153
	2003 Nov 17	2961	1.068	−142
	2004 Mar 6	3071	1.122	−29

NOTES.—Observations made with the G430M or G750M grating. All *HST* STIS spectra used in this analysis are available at http://archive.stsci.edu/prepds/etacar/ or http://etacar.umn.edu.
[a] Phase relative to the beginning of the *RXTE* low state 1997.9604: JD 2,450,799.792+2024 × ϕ (Corcoran 2005).
[b] *HST* GO Program (PI: K. Davidson).
[c] STIS GTO Program (PI: T. R. Gull).

and [N II] $\lambda 5756$ (N I IP 14.5 eV with N II IP 29.6 eV). Due to the large abundance of hydrogen and its IP, H I lines form throughout the stellar wind structure. Iron shows similar behavior to hydrogen, but due to its ionization structure, Fe II lines form in the outer lower excited regions of η Car A's wind, with the interior region dominated by more highly ionized iron. Helium is mainly neutral in the environment of the primary star. However, the energy level structure (see Fig. 1) is such that high-energy photons are required even to populate the lowest excited states. He I lines represent the highly excited regions of the stellar wind or the bow shock. The [N II] $\lambda 5756$ line is a parity forbidden line and is thus formed in the outer, low-density, ionized region.

STIS optical spectra of the star show that the excited He I stellar lines are peculiar relative to lower excitation wind lines: the He I lines are blueshifted relative to the system velocity (-8 km s^{-1}; Smith 2004) over most of the 5.54 yr cycle, unlike the lower excitation lines, whose emission is centered near system velocity. The He I P Cygni lines in the η Car spectrum are characterized by broad asymmetric P Cygni profiles that often exhibit multiple, discrete peaks. Another unusual characteristic of the He I lines is the abrupt, large velocity shift toward the system velocity, exhibited in both emission and absorption, which occurred during the 2003.5 minimum. The variations of the He I P Cygni lines in both strength and radial velocity suggest that most of the He I lines are influenced by the ionizing flux of the companion star (Hillier et al. 2006).

While the spectrum of η Car is rich in wind lines, many lines are not suitable for detailed analysis. A large number of He I lines are located in the STIS CCD spectral range (1600–10300 Å), but many, such as the commonly used He I $\lambda 4473$, are either blended or too faint for reliable interpretation. Even with the 0.152″ extraction, a few of the lines are influenced by emission from the

surrounding nebula and the Weigelt blobs. The He I $\lambda\lambda 5877$, 6680 lines are slightly affected by narrow, nebular [Fe II] and [Ni II] emission lines, respectively. The least contaminated He I transition in the spectrum, for both absorption and emission, is He I $\lambda 7067$. Hence, we use this spectral line to illustrate the variability in absorption and emission. Unfortunately, the absorption in He I $\lambda 7067$ is often weak and difficult to measure. We have therefore also utilized the absorption portion of He I $\lambda 5877$. The He I $\lambda 5877$ line has the same lower state as He I $\lambda 7067$, but its oscillator strength is almost 1 order of magnitude greater and its absorption is correspondingly stronger. The He I $\lambda 5877$ emission is heavily affected by the strong Na I $\lambda 5892$ resonance absorption from the stellar wind, the intervening ejecta, and the interstellar medium. The He I $\lambda 5017$ line is badly blended with Fe II $\lambda 5020$, and consequently little information can be gleaned about the emission profile. However, we can estimate the influence of the blend on the associated absorption using other members of the same multiplet, such as Fe II $\lambda 5170$. We find that the absorption is dominated by the He I component throughout most of the period but is overwhelmed by Fe II absorption for a short interval after periastron (§ 4.1). A complete set of lines used in this analysis is presented in Table 2, while a detailed discussion of a subset of the least blended transitions is presented in § 4.

To investigate the strongly phase-dependent and complex profile variability, we utilized a variety of techniques. To illustrate these, we use He I $\lambda 7067$, which shows strong variability at all phases. At least four components can be identified in He I $\lambda 7067$: one absorption component, two narrow emission components that give rise to the bulk of the observed emission, and a much weaker, broad emission component. All these components show significant time variability.
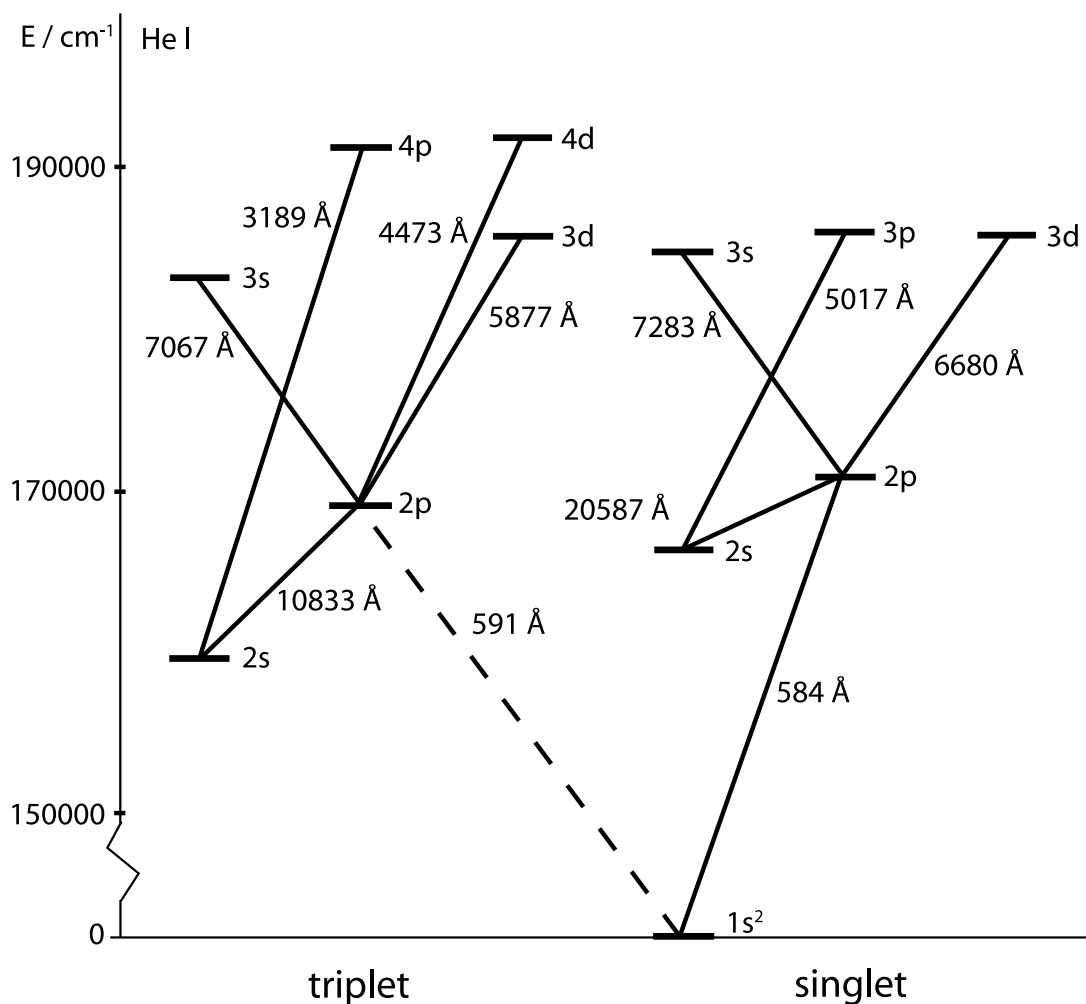
FIG. 1.—Energy level diagram including all He I transitions used in this analysis. Note the amount of energy needed to populate the excited states ($1 \text{ cm}^{-1} = 1.240 \times 10^{-4}$ eV). All wavelengths are in vacuum.

To illustrate the observed spectral variations, we stacked continuum-normalized line plots in velocity space (Fig. 2). We also used a color-coded intensity plot to illustrate the variation as a function of orbital phase. We created the color-coded plots by stacking the spectra according to phase, normalizing to the flux at -1200 km s^{-1} relative to the vacuum rest wavelengths of the wind lines, where the continuum is seen to be unaffected by the wind line variations. The flux between the observations has been calculated by interpolation in phase to help identify systematic trends. The normalization procedure is used for the visualizations only and utilized to emphasize the spectral variations with phase. The systematic change in radial velocity is apparent, as is a discontinuity in the radial velocity of the He I absorption near phase 1.0 (Fig. 3). Quantifying the observed spectral changes is difficult, since both the shape and strength of the line change. In addition, reliable measurements of absolute line fluxes are difficult since the amount of extinction is declining with time. Since 1997, the brightness of the central star, as observed by *HST* in Hα, has increased by over a factor of 3 (Martin & Koppelman 2004). During the minimum, small variations (10%–20%) in continuum flux levels occur (Martin & Koppelman 2004; Feast et al. 2001), and the variations are not likely to be associated with a variation in dust extinction.

The P Cygni wind profile of a single massive star can be described by emission originating throughout the wind with absorp-

tion of the background emission in line of sight toward the observer. For a binary system the wind profiles are more complex due to excitation and motion of the companion star. In the case of η Car, lines such as in H I and Fe II are formed throughout the dominating primary wind. In the absence of a companion star, the He I P Cygni lines must form in a high-excitation zone close to the primary star. With a companion present, significant He I emission can arise in an ionized region near the bow shock, and hence at much larger radii. The structure is even more complex due to the highly eccentric binary orbit ($e \sim 0.9$). The Coriolis effects lead to a highly distorted emission structure, especially near periastron passage. By contrast, the He I absorption arises from a confined but asymmetric region in line of sight from the primary stellar source. Consequently, we have chosen to use the P Cygni absorption component in our analysis. To determine the radial velocity variation of the absorption components, we have fitted multiple Gaussians to the line profiles, as illustrated in Figure 4. With this fitting procedure additional emission components are needed, which do not necessarily indicate spatially distinct emitting regions. The specific number of the narrow components used in the fit is chosen to mimic the general shape of the emission line and, as far as possible, to decouple the emission from the absorption. The number of narrow components needed to fit each line profile changes with phase but is consistent for all lines at a given phase. The accuracy of the measured radial velocity is phase dependent, due to a weak

TABLE 2
Spectral Lines Used in This Analysis

Spectrum	λ_{vac} (Å)	Transition	E_{low}[a] (cm^{-1})	E_{up}[a] (cm^{-1})	log gf
He I[b]	3188.67	$2s\ ^3S-4p\ ^3P$	159856	191217	−1.16
	4472.73	$2p\ ^3P-4d\ ^3D$	169087	191445	0.05
	5017.08	$2s\ ^1S_0-3p\ ^1P_1$	166278	186209	−0.82
	5877.31	$2p\ ^3P-3d\ ^3D$	169087	186102	0.74
	6680.00	$2p\ ^1P_1-3d\ ^1D_2$	171135	186105	0.33
	7067.20	$2p\ ^3P-3s\ ^3S$	169087	183237	−0.21
	7283.36	$2p\ ^1P_1-3s\ ^1S_0$	171135	184865	−0.84
H I[c]	3723.00	$2s-14p$	82259	109119	−1.98
	3735.43	$2s-13p$	82259	109030	−1.87
	3751.22	$2s-12p$	82259	108917	−1.76
	3771.70	$2s-11p$	82259	108772	−1.64
	3798.98	$2s-10p$	82259	108582	−1.51
	3836.47	$2s-9p$	82259	108324	−1.36
	4102.89	$2s-6p$	82259	106632	−0.75
	4341.68	$2s-5p$	82259	105292	−0.45
	8865.22	$3s-11p$	97492	108772	−1.05
	9017.39	$3s-10p$	97492	108582	−0.90
Fe II[d]	5019.84	$4s^2\ a^6S_{5/2}-4p\ z^6P_{5/2}$	23318	43239	−1.35
	5170.47	$4s^2\ a^6S_{5/2}-4p\ z^6P_{7/2}$	23318	42658	−1.25
N II[b]	5756.19	$2p^2\ ^1D_2-2p^2\ ^1S_0$	15316	32689	−8.24

Notes.—Energy levels and wavelengths for H I and the He I triplets are weighted averages due to multiple unresolved transitions. The log gf is a sum over all transitions in the multiplet. All wavelengths are in vacuum.

[a] 1 cm^{-1} = 1.240×10^{-4} eV.
[b] Atomic data from http://physics.nist.gov/ PhysRefData /ASD/index.html.
[c] Atomic data from Kurucz (1988).
[d] log gf from ftp:// ftp.wins.uva.nl /pub/orth /iron/ FeII.E1; all other atomic data from Kurucz (1988).

absorption or the possible presence of multiple components. Typical residuals to multi-Gaussian fits were less than 2%.

4. LINE PROFILE VARIABILITY

The line profiles in the η Car spectrum exhibit a wide variety of shapes and variability. Below we discuss the general characteristics and observed changes.

4.1. He I *Profiles*

The He I line profiles are complex and appear to be a composite of multiple features. The profiles change considerably between observations, especially in the phase interval $0.85 < \phi < 1.20$ (Figs. 2 and 3). On top of a broad weak emission are relatively narrow emission components that change rapidly with time. All spectral line characteristics (i.e., strength, shape, and radial velocity) vary systematically with phase. For each observation, the He I profiles are shifted to the blue relative to the position of the H I lines (compare Figs. 2 and 3 with Figs. 5 and 6). While both the H I emission and He I emission weaken during the minimum, the velocity shift for the He I emission is pronounced, and much larger than the corresponding shift observed in H I (see § 4.2). We observe these shifts especially on the red side of the emission line where the profile is unperturbed by the blueshifted absorption. With phase, the He I emission increasingly shifts to the blue until just before the X-ray low state begins. Between phases 0.995 and 1.013, the intensity of the emission abruptly drops and the centroid of the emission line shifts to more positive velocities. After the minimum the emission is gradually more blueshifted. At some epochs the profile is nearly symmetric, while at others the profile shows two or more narrow peaks. The limited sampling of this varying profile, as well as possibly spatially limited res-
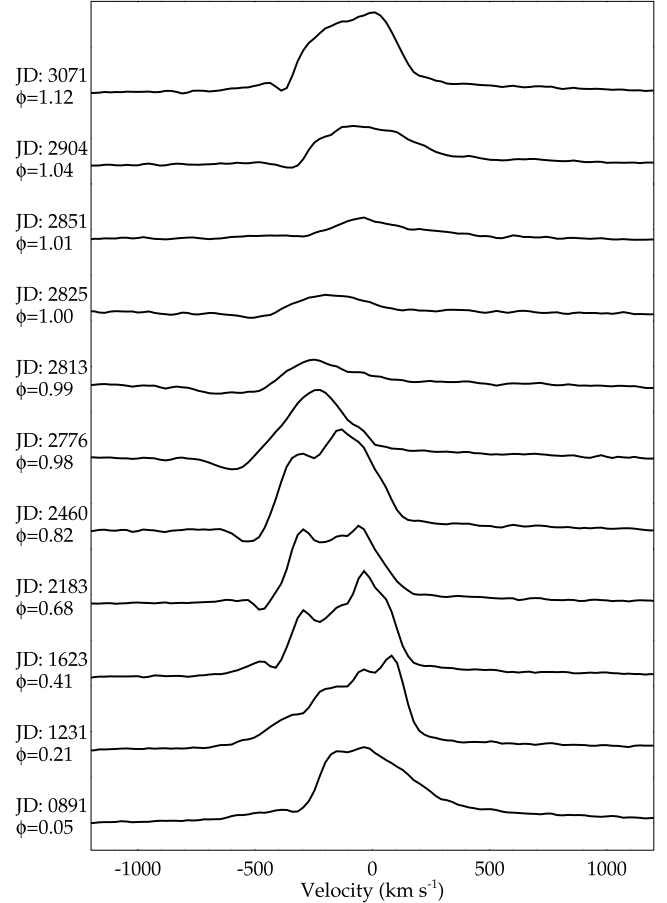

Fig. 2.—He I λ7067 profiles from 1998.0 to 2004.3. The He I lines profiles, mostly blueshifted relative to the −8 km s^{-1} system velocity, are asymmetric and vary in intensity and velocity with phase. The 2003 June 23 (Julian Day 2,452,813 = JD: 2813) observation shows greater absorption at higher velocities ($v \sim -800$ km s^{-1}) than any of the other observations. This large blueshift is due to a second absorption system at higher velocity. At phase $\phi = 0.21$, the absorption is weak and the velocity measurement is uncertain.

olution, complicates the interpretation of the emission-line radial velocities. Detailed modeling and possibly higher spatial/spectral resolution are required for a quantitative interpretation of the velocity variations.

The He I absorption components vary in velocity and strength and are traceable over η Car's entire 5.54 yr spectroscopic period. The absorption velocity varies systematically (except between $\phi = 0.0$ and 0.2) with a discontinuous jump of more than 200 km s^{-1} near periastron (Fig. 7).

In Figure 8 we show the measured absorption radial velocities for He I $\lambda\lambda$5877, 6680, 7067, 7283. The behavior previously discussed can be observed in all the lines. However, there is scatter in the radial velocity measurements of different lines at the same phase. The absorption in He I and H I, apparent in Figures 3 and 6, is strongest at different phases. The He I absorption is strongest in the phase interval $0.8 < \phi < 1.0$, and relatively weak at other phases. Conversely, the H I P Cygni absorption, particularly of the Balmer series members, strengthens after $\phi = 0.98$, is extremely strong at $\phi = 1.0$, and weakens after the minimum.

Damineli et al. (2000) investigated the variability in He I λ6680 emission using ground-based, seeing-limited spectra. They concluded that the changes with phase were caused by excitation effects rather than motion of either of the objects in the binary system. The velocity amplitude measured in He I λ6680 emission by Damineli et al. (2000) is in qualitative agreement with our
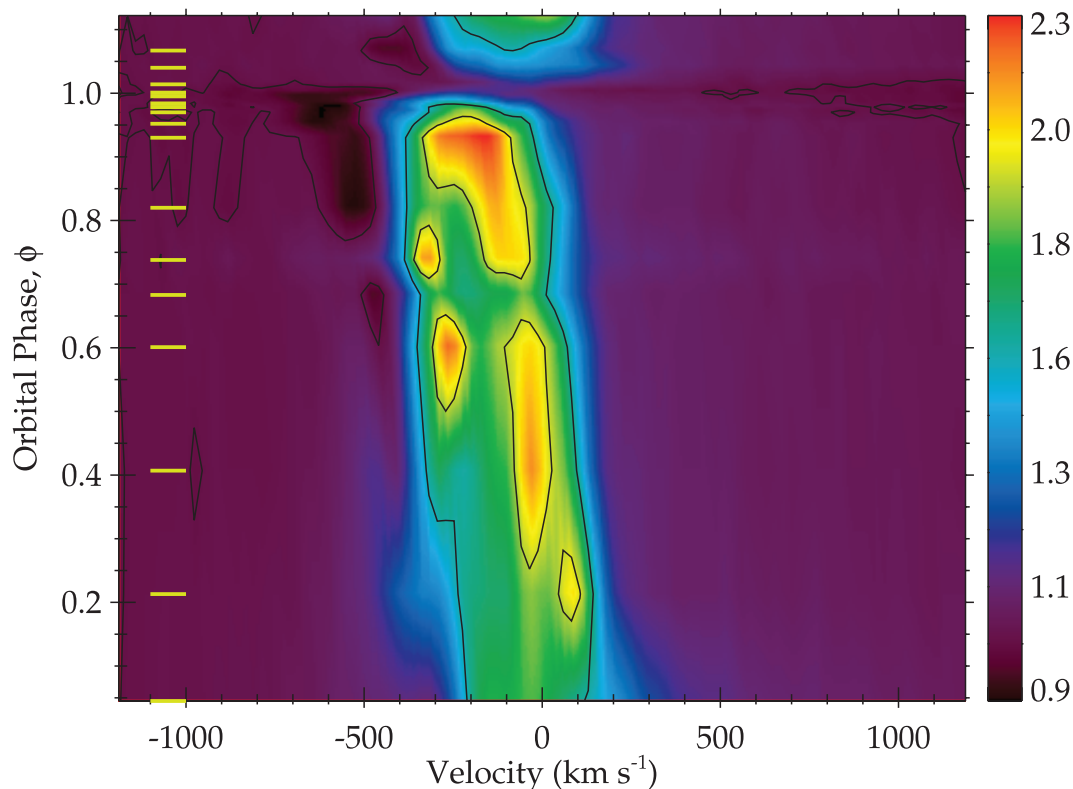
FIG. 3.—Surface plot for He I λ7067. The line profile's variation with phase is presented with the intensity color-coded from black to red with increasing line emission. All spectra used in the figure have been normalized to the flux at −1200 km s⁻¹. The observed phase points are marked to the left in the figure. Notice that the two emission components merge just before periastron with a distinct velocity shift at phase $\phi = 1.0$ (2003 June 29). The absorption, in contrast to that shown by H I, is most prevalent at $\phi = 0.8$–1.0. The contours represent the flux level at −1200 km s⁻¹ plus 0.70 and 0.85 of maximum line emission.
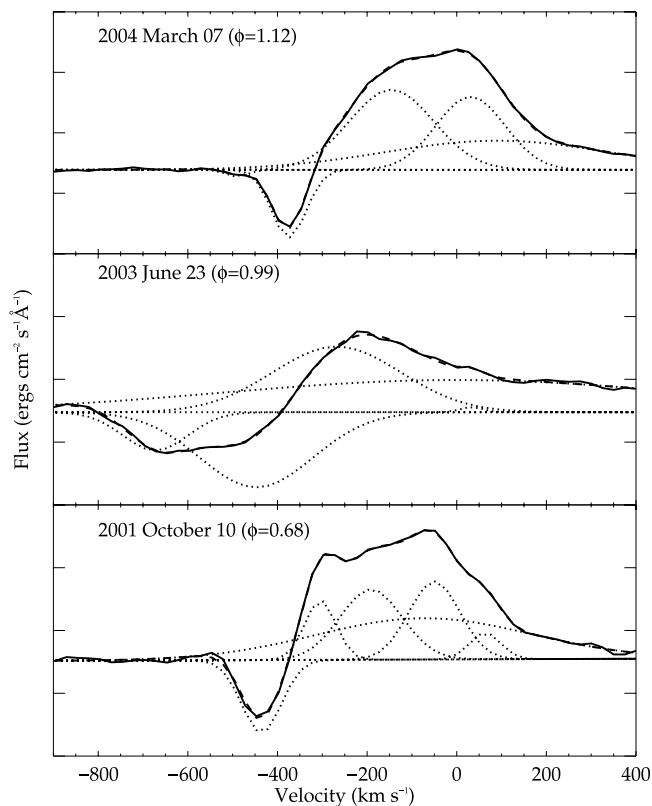
FIG. 4.—He I lines can be described by a broad P Cygni wind profile with the superposition of several narrow emission components as exemplified with the He I λ7067 profiles and component fits. Solid line: Observed spectrum. Dashed line: Fitted line profile based on a sum of the individual components (dotted lines).

observations. However, the results from the Damineli et al. (2000) analysis are based on variability in emission-line strength, while our results originate from absorption-line radial velocities. The results may not be directly comparable but do show similar results regarding the amplitude and overall characteristic of the radial velocity curve.

The relative strength of the He I triplet lines to the singlet lines (see Fig. 9) provides information on whether the lines are formed by photoexcitation or photoionization/recombination processes. An important question for understanding the origin of the He I absorption is what determines its strength: is it primarily due to optical depth effects, or does the fractional coverage of the continuum-emitting source also play a role?

We comment on the He I lines that can or cannot be studied in the η Car spectra covered by STIS:

1. Absorption from the metastable state $1s2s\ ^3P$. All observable transitions from this term are severely blended. He I λ3889 is, for example, blended with H I λ3890.

2. Absorption from $1s2s\ ^1S$, such as He I λ5017. This line is blended with Fe II λ5020. However, the effect of the Fe II line can be determined using Fe II λ5170 as Fe II λλ5020, 5170 have the same lower energy state. Since the gf-value for Fe II λ5170 is similar to that of Fe II λ5020, absence of significant absorption in Fe II λ5170 for any specific observation indicates that the absorption associated with Fe II λ5020 is due to the He I line. From $\phi = 0.2$ to 1.0, the He I contribution dominates the absorption, which is reasonable since the $1s2s\ ^1S$ is a long-lived state. Late in this interval, the absorption depth exceeds 50%, indicating that a significant fraction of the background-emitting region is covered by He I gas responsible for the absorption. Unfortunately, from $\phi = 0.0$ to 0.2 and from 1.0 to 1.2, the Fe II component becomes
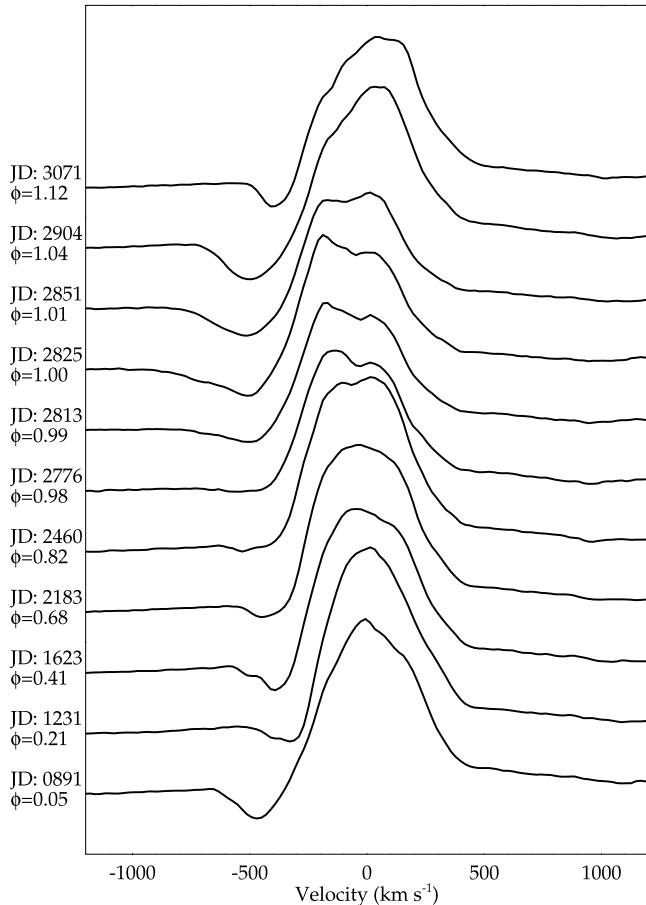
Fig. 5.—H I λ4103 variability in intensity and velocity over the spectroscopic period. The emission centroid and emission fluxes are close to the system velocity (-8 km s^{-1}), and it and the emission fluxes do not generally undergo the dramatic changes observed in He I. However, significant changes in the emission-line radial velocity and the H I emission line strength occur near phase $\phi = 1.0$. Changes are observed in the P Cygni absorption over the entire cycle, with the absorption weakest at $\phi = 0.21-0.98$. The absorption velocity varies over the period but with a smaller amplitude than observed in He I.

strong while, as shown by other He I lines, the He I λ5017 absorption weakens. Hence, He I λ5017 cannot be used to trace the He I absorption across the minimum. Absorption associated with He I is seen on He I λ3966, which is a similar transition as He I λ5017, but this line is severely blended.

3. Absorption from $1s2p\ ^3P$, including He I $\lambda\lambda$4473, 5877, 7067, where He I λ5877 is the strongest. The strength of the absorption lines is partially controlled by optical depth effects and not dominated by effects related to partial coverage of the continuum source.

4. Absorption from $1s2p\ ^1P$, including He I $\lambda\lambda$4923, 6680, 7283. He I λ6680 is the least contaminated, but He I λ7283 is usable in this analysis.

Analysis of the He I absorption shows that at some phases, the He I in the He$^+$ zone absorbs much of the flux from the back-illuminating source, η Car A. For example, on 2002 July 4 ($\phi = 0.820$), the central intensity in He I λ5017 is less than 50% of the adjacent continuum level. We note that the line absorption equivalent widths do not vary uniformly. There is a significant difference in variation between lines as shown in Figure 9, where the equivalent widths of He I λ6680 (singlet) and He I λ7067 (triplet) are compared. A significant change in their relative strengths occurs around $\phi = 0.9-1.1$, indicating changes of the physical conditions of the absorbing regions. Figure 9 shows a greater

equivalent width for He I λ7067 near periastron compared to He I λ6680, indicating ionization/recombination to be the major mechanism for populating the He I energy states when η Car B is close to η Car A.

We created radial velocity curves for the He I absorption (Fig. 8) in He I $\lambda\lambda$5877, 6680, 7067, 7283 and a mean radial velocity curve (Fig. 7). As with the peak absorptions, the most blueshifted of He I and H I occur at different phases. The greatest blueshift for He I occurs leading up to the X-ray low state ($\phi = 1.0$). In comparison, the greatest blueshifts for H I and Fe II occur during and post-minimum and are noticeably less than observed in the He I lines.

4.2. H I *Profiles*

We use H I λ4103 (Hδ) to best illustrate spectral variations in hydrogen. This is a moderately intense, unblended line and is influenced by radiative transfer effects in a less complicated way than Hα. The Hδ line, as presented in Figures 5 and 6, shows phase-dependent variations in both emission and absorption. The Hδ emission component varies substantially less than observed in He I (see § 4.1). Normalized to the continuum flux, the H I lines do not vary greatly in intensity, although a change occurs close to periastron ($\phi = 1.0$), where the peak emission in Hδ drops by approximately 30%. This behavior has previously been discussed by Davidson et al. (2005), where it was interpreted as evidence of a shell ejection event. During the minimum, the Hδ profile is flat topped ($\phi = 1.01$ in Fig. 5), unlike profiles observed at other phases. One reason for invoking a shell ejection is that a similar line profile was not observed during earlier spectroscopic minima. An alternative explanation is that η Car exhibits long-term mass-loss variations and that these are superimposed on the phase-related variations. The velocity variation of the emission is small (<25 km s^{-1}), except between phases 0.9 and 1.1, and is illustrated by the stable behavior of the red side of the emission profile. The velocity shift observed on the red portion of the H I lines is, however, dependent on a good understanding of the continuum and the spectral line shape. The measurements of the position of the absorption component yield a velocity amplitude of $\sim$60 km s^{-1}. In an earlier study Damineli et al. (2000), using ground-based spectra, derived a radial velocity curve using a large number of velocity measurements in H I Paγ and Paδ. They derived a velocity amplitude of 50 km s^{-1}, centered at the systemic velocity. However, their orbital solution was, according to Davidson et al. (2000), inconsistent with higher spatial resolution *HST* spectra. A major difficulty in interpreting the velocity shifts in the hydrogen lines occurs because the P Cygni profile is confused in ground-based data, by nebular scattered radiation and emission from the Weigelt blobs.

The major part of the H I emission is formed in the extended wind of η Car A. Some of the variations and structure seen on top of the broad emission may arise from asymmetries in the primary wind, or alternatively from changes in emission from the bow shock associated with the wind-wind collision. Similarly, velocity variations could be due to the motion of η Car A, or to changes in the wind structure. In both cases the observed amplitude of the velocity variations will be reduced since the H I–emitting region is extended well beyond η Car B's orbit. Consequently, it takes a finite time to replenish the gas. In the model of Hillier et al. (2006) roughly 50% of the emission originates beyond $R \sim 1500\ R_\odot$. A characteristic flow time (R/v_A) is thus 25 days, assuming $v_A = 500$ km s^{-1}, which is η Car A's terminal wind velocity. Recombination timescales are much shorter.

In contrast to the emission, the H I P Cygni absorption is highly variable. At some phases (e.g., just after $\phi = 1.0$) the absorption is strong, while at other phases ($0.50 < \phi < 0.95$) it is much
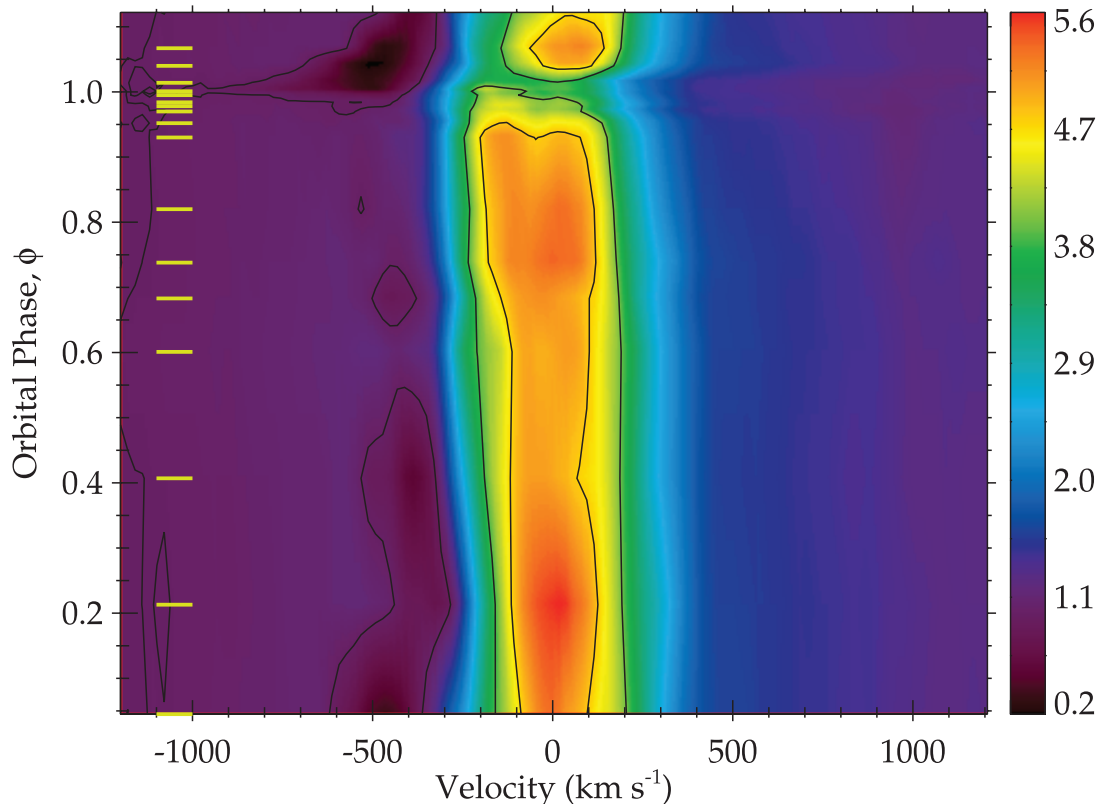
FIG. 6.—Surface plot for H I λ4103. The line profile's variation with phase is presented with the intensity color-coded from black to red with increasing line emission. All spectra used in the figure have been normalized to the flux at -1200 km s^{-1}, and the phase points are marked on the left of the figure. The emission profiles are nearly constant, in both intensity and velocity, throughout most of the period. Significant changes are seen in the emission profile near phase $\phi = 1.0$; there is a reduction in flux and a velocity shift. An abrupt strengthening of the P Cygni absorption occurs after phase $\phi = 1.0$. The contours represent the flux level at -1200 km s^{-1} plus 0.70 and 0.85 of maximum line emission.
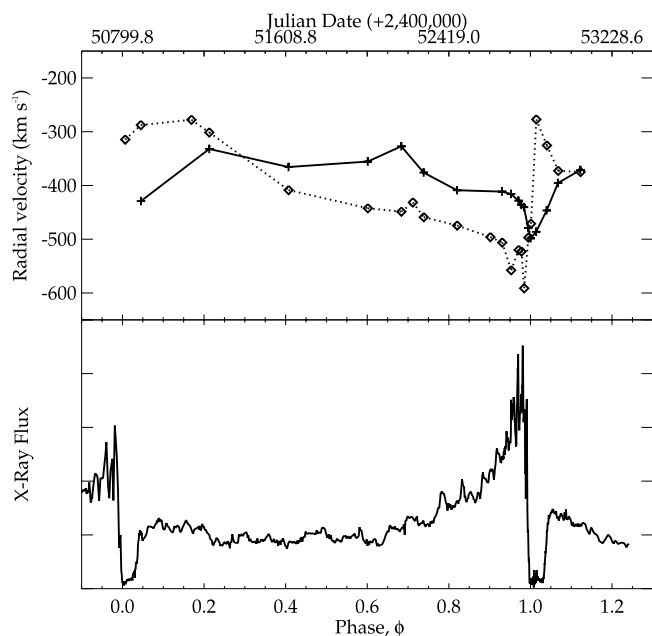
weaker, and in some lines difficult to detect. For Hδ the most striking behavior of the P Cygni absorption is the rapid strengthening near $\phi = 1.0$. At $\phi = 0.984$ (2003 June 1) no absorption can be seen in Hδ, while it is marginally detectable on Hα. By $\phi = 0.995$ (2003 June 22), the absorption increased dramatically. P Cygni absorption can be seen on high-n members of the Balmer series (Fig. 10) at all epochs observed with *HST* STIS.

The H I absorption shows radial velocity variations across the period (Figs. 6, 7, and 10). During most of the period, the H I absorption velocity typically is between -330 and -400 km s^{-1} but varies substantially around periastron. In the phase interval $0.95 < \phi < 1.20$, the absorption radial velocity falls from approximately -400 to -500 km s^{-1}, before recovering to its pre-minimum level.

4.3. Fe II *Profiles*

The Fe II profiles also show intensity and radial velocity variability. To illustrate the Fe II variability, we use Fe II λ5170 (see Fig. 11), which is one of the stronger Fe II wind lines in the optical spectrum of η Car. According to models of luminous blue variables (LBVs) like η Car, the Fe II emission is primarily produced by continuum fluorescence (e.g., Hillier et al. 1998, 2001). This line provides a useful comparison to the He I λ5017 + Fe II λ5020 feature (Fig. 12). The third member of the multiplet, Fe II λ4925, shows a similar emission profile as Fe II λ5170 at all phases.

Radial velocity variations are difficult to measure since the profile shows marked variability on the blue side. While some of this variability appears to be directly related to the P Cygni
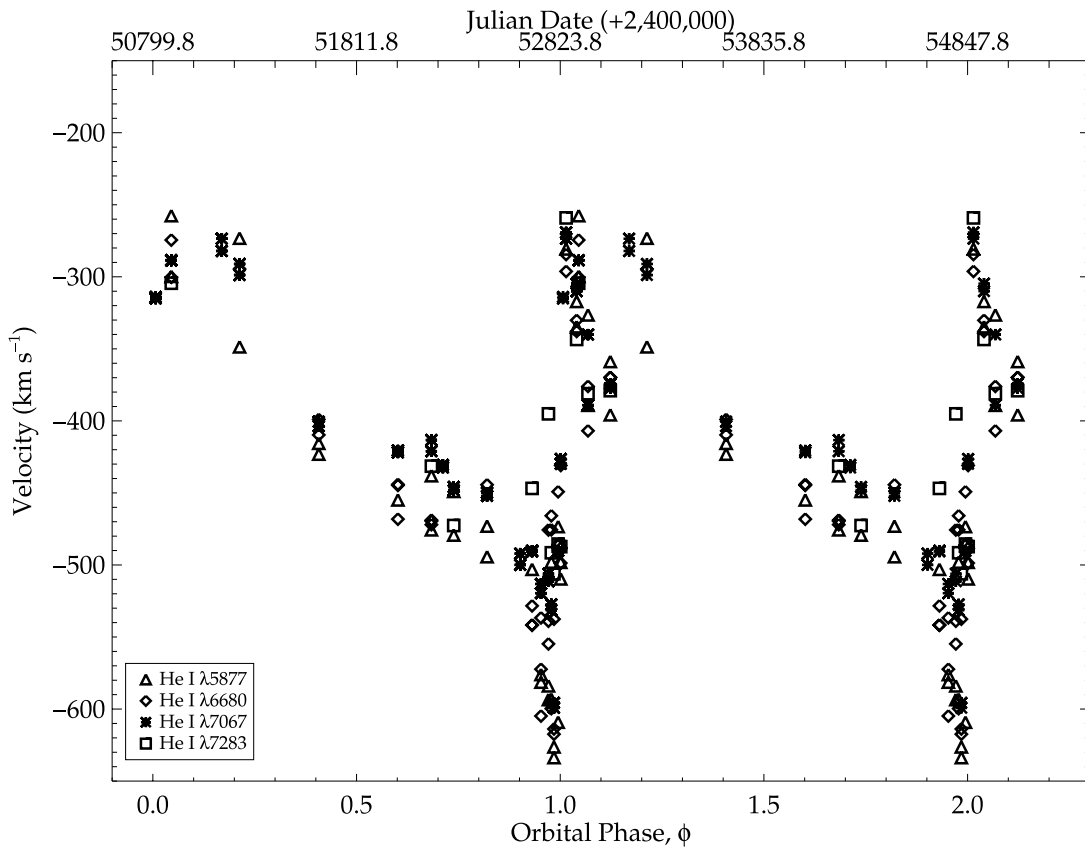

FIG. 7.—*Top*: Radial velocities measured for the He I absorption (*diamonds and dashed line*) and H I (*plus signs and solid line*). Note the dramatic velocity shift for the He I lines after periastron ($\phi = 1.0$). *Bottom*: X-ray light curve from Corcoran (2005).

FIG. 8.—Radial velocities for the He I absorption. The typical measurement error is ~20 km s^{-1}. Data points recorded between 0 and 1.2 are replotted one period later to show periodic variability.
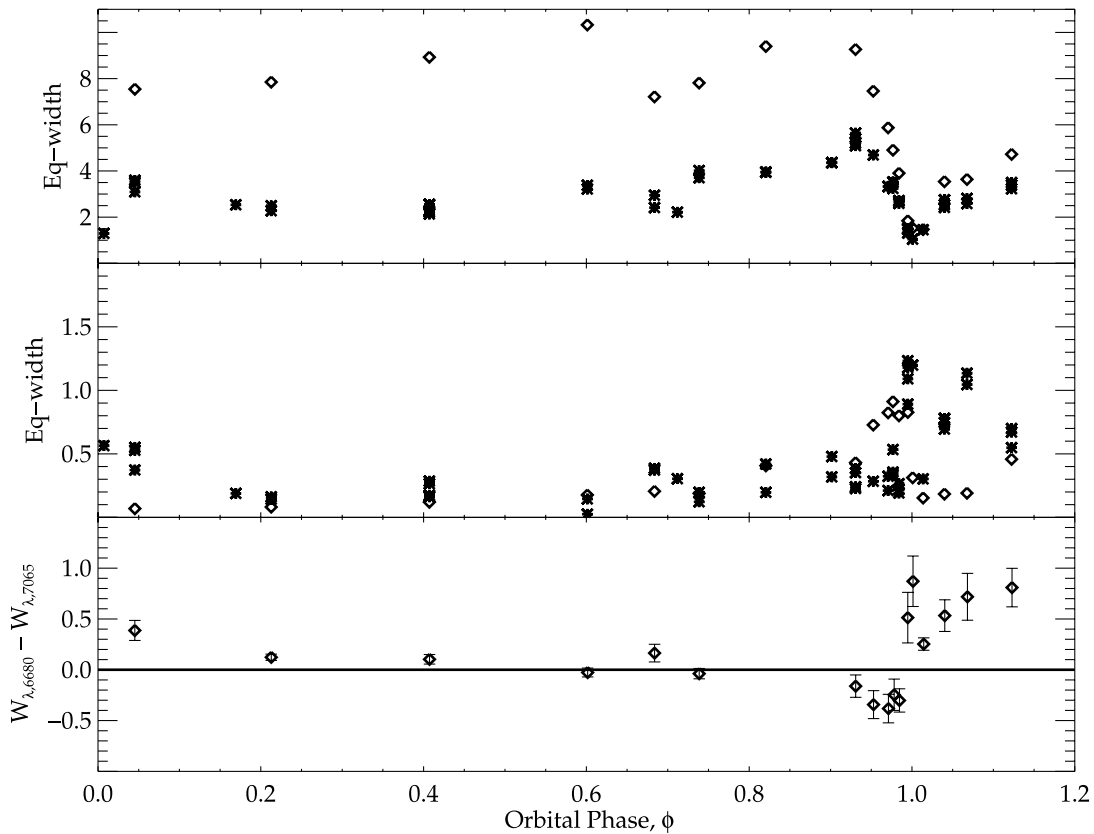

FIG. 9.—*Top*: Emission equivalent widths for He I $\lambda\lambda$6680, 7067. *Middle*: Absorption equivalent width for He I $\lambda\lambda$6680, 7067. He I λ6680 is shown by asterisks and He I λ7067 by diamonds. *Bottom*: Difference in absorption equivalent width as a function of phase. Error bars on the data points represent a 20% uncertainty in measurements for each of the two lines. The shift over the spectroscopic cycle indicates a change in dominant excitation mechanism. During periastron an increase of equivalent width in He I λ7067 (triplet) relative to He I λ6680 (singlet) indicates more ionization/recombination relative to photoexcitation.
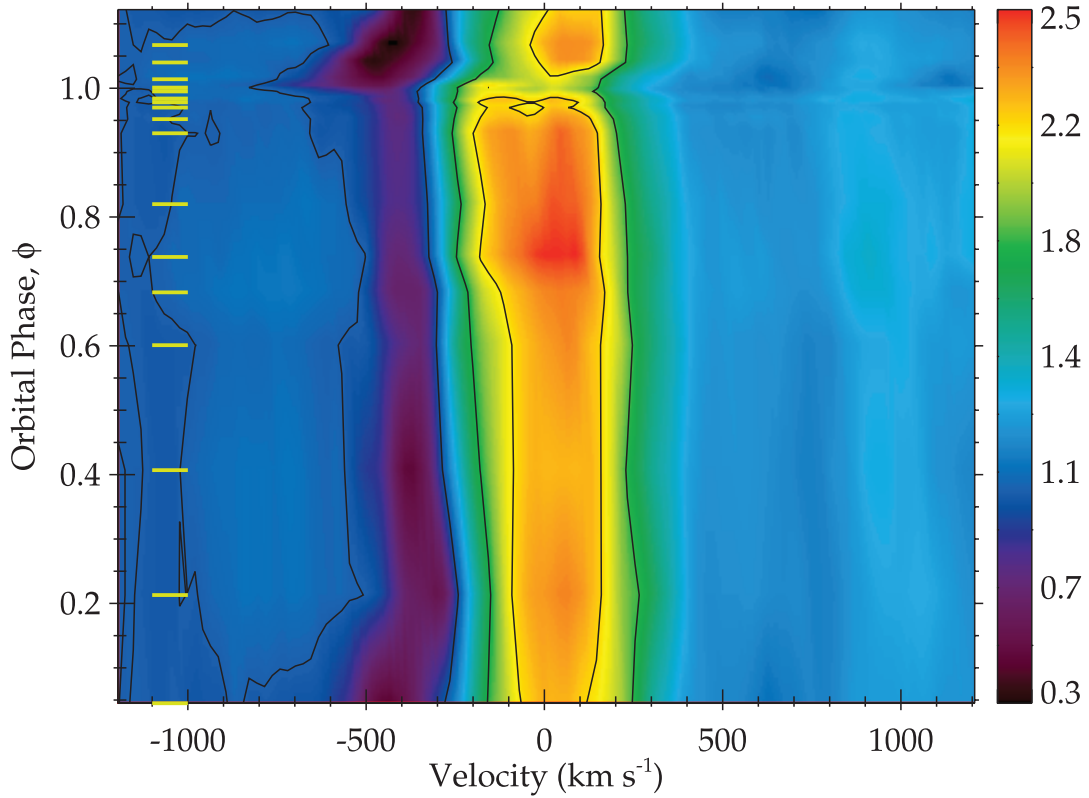
FIG. 10.— Surface plot for H I λ3836. In contrast to H I λ4103, P Cygni absorption is readily detectable at all phases. Like H I λ4103, and in contrast to the He I lines, the H I λ3836 emission profile and radial velocity are relatively constant. Near $\phi = 1.0$, the emission profile weakens significantly with an associated velocity shift. The contours represent the flux level at -1200 km s^{-1} plus 0.70 and 0.85 of maximum line emission.
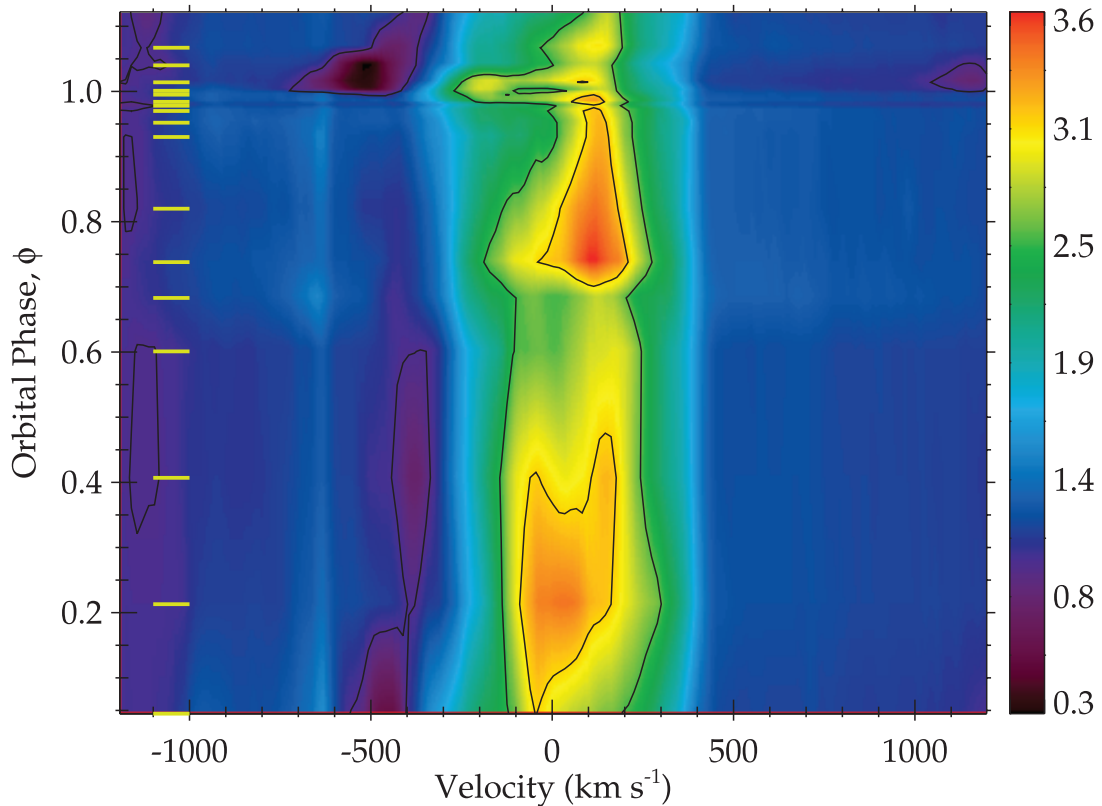

FIG. 11.— Illustration of Fe II λ5170 variability in intensity and velocity over the spectroscopic period. The absorption component and emission on the blue side are strongly variable with phase. Conversely, emission on the red side is relatively stable in strength and in radial velocity. The contours represent the flux level at -1200 km s^{-1} plus 0.7 and 0.85 of maximum line emission.
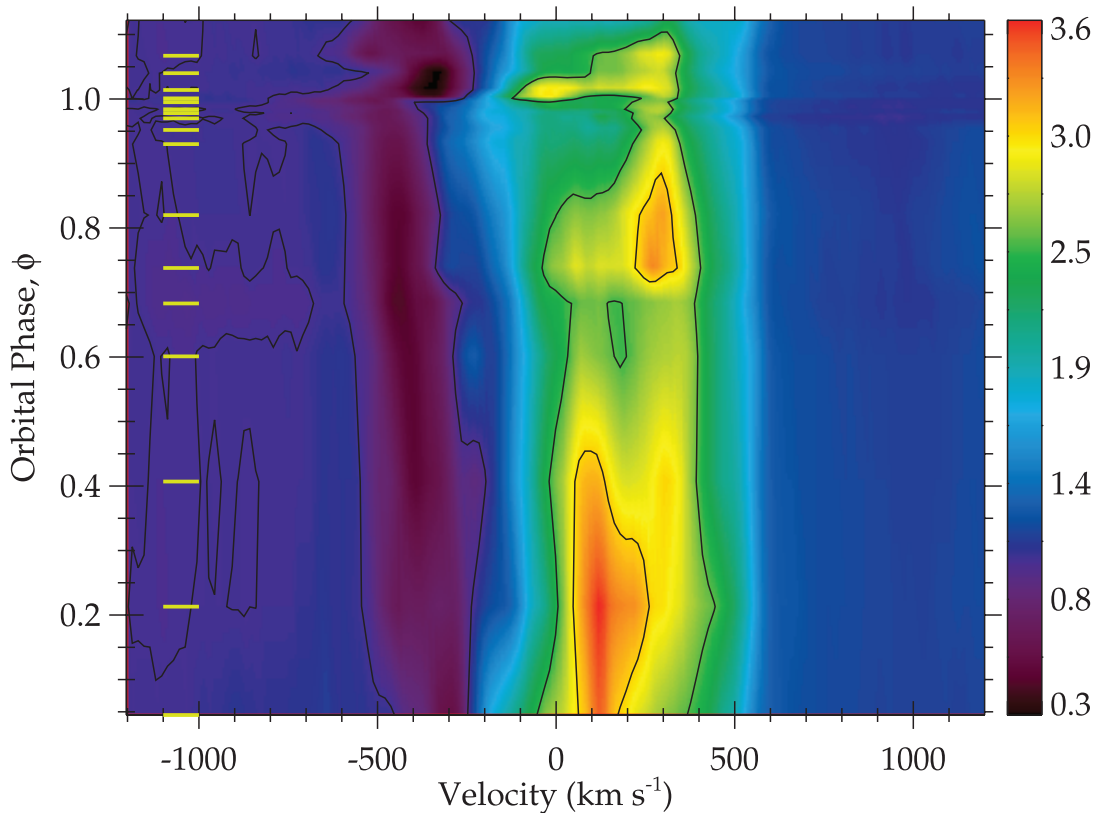
F_{IG}. 12.—Illustration of He I λ5017, which is blended with the stronger Fe II λ5020. The velocity scale is for He I λ5017. Fe II λ5020 has the same lower level as Fe II λ5170 (Fig. 11) and belongs to the same multiplet. Comparison shows that absorption in the He I component dominates between $\phi = 0.2$ and 1.0. The contours represent the flux level at -1200 km s^{-1} plus 0.70 and 0.85 of maximum line emission.

absorption, much of it can be associated with change in the emission on the blue side. Conversely, the red side of the profile, with the exception of the spectrum recorded at phase 0.21 (1999 February 21), shows minimal variability, with the velocity changes typically being less than 20 km s^{-1}. Similar to the H I line profiles, the Fe II absorption components are weak throughout most of the 2024 day cycle. They begin to strengthen around $\phi = 0.98$, are strong just after periastron ($\phi = 1.0$), but have virtually disappeared at $\phi = 1.2$.

Given the strength of the Fe II emission in the η Car spectrum, the weak P Cygni absorption in all profiles of lines in the multiplet, including Fe II $\lambda\lambda$5020, 5170, throughout the broad maximum is difficult to explain with a spherically symmetric model. At times, the Fe II emission is double peaked, while at other occasions the blue side of the profile is severely weakened relative to the red side.

The spectral behavior observed in Fe II can indicate distinct emitting regions, one of which is highly variable. Alternatively, the bulk of the Fe II emission could come from the primary stellar wind. Variations would then be explained by significant perturbations to the ionization structure of the wind region that affects the blueshifted emission. Such a scenario is consistent with a hot companion star ionizing the wind on the observer's side of η Car A.

4.4. [N II] Profiles

The [N II] λ5756 line shows a complex structure with multiple narrow emission peaks spanning velocities of -500 to $+500$ km s^{-1} (Figs. 13 and 14). This line profile is significantly broader than the He I emission lines and is centered about the -8 km s^{-1} sys-

tem velocity. Near $\phi = 1.0$ the emission is weak, with the observed line representing intrinsic [N II] emission from the primary wind. At other phases the emission is stronger, more structured with the emission weighted toward the blue. Such emission can arise due to additional ionization of the primary wind by η Car B or line formation in the bow shock. At phases 0.21 and 0.68 the [N II] profiles differ substantially from those in He I. The emission is more heavily weighted to the blue side. The [N II] emission components show little or no velocity variation; only the intensity of individual components changes with orbital phase. The lack of velocity variation indicates that the [N II] emission is formed beyond the inner, denser portions of the primary wind or the wind-wind collision region. The [N II] emission, as with numerous [Fe II] lines and other forbidden line species, originates in lower density, outer wind regions. Using the model of Hillier et al. (2001), the extended [N II]–emitting region coincides with, and extends well beyond, the binary orbit (semimajor axis $\sim$15 AU). While the critical density of the ^1D state is approximately 8.6×10^4 cm^{-3} at 10^4 K (Osterbrock & Ferland 2006), most of the emission may come from larger particle densities if hydrogen has already recombined.

5. SINGLE STAR SHELL EJECTION VERSUS BINARY-DRIVEN VARIABILITY

A proper interpretation of the line profile variability depends on the excitation mechanisms in the line formation region. Since η Car is considered to be an LBV, a natural interpretation is that the observed emission- and absorption-line variations are evidence for periodic shell ejections. Shell ejections were invoked, for example, by Zanella et al. (1984) to explain the observed variation
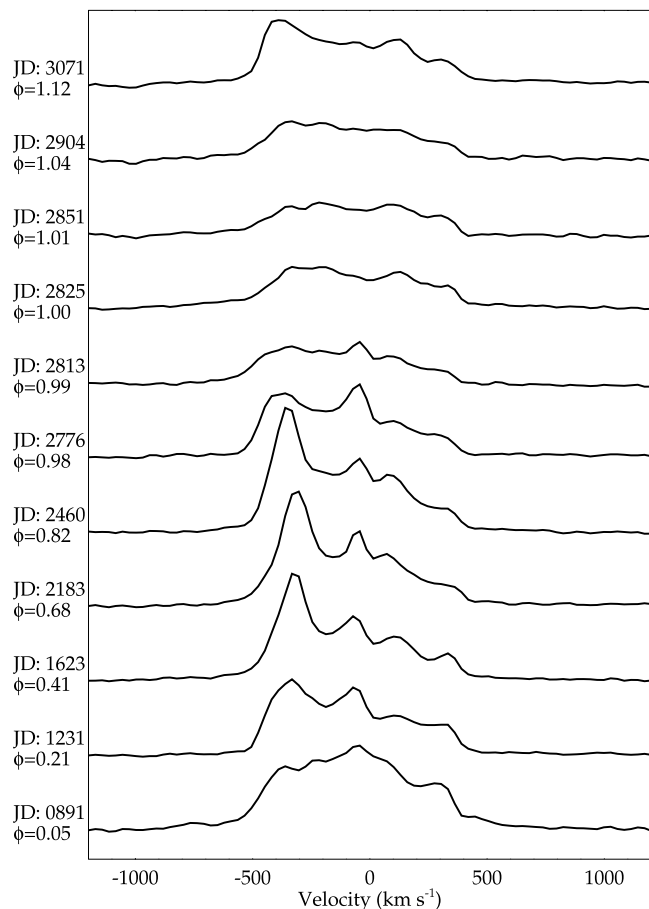
Fig. 13.—[N II] λ5754 variations over the spectroscopic period. The line profile is asymmetric and can be described with four narrow components that mutually vary in intensity but not in velocity with phase. The line is centered near the −8 km s⁻¹ system velocity. There may be a broad underlying component associated with the stellar wind.

of high-excitation features seen in ground-based spectra. The discovery of the 2024 day period suggested that the variations could be explained by orbital modulation in a binary system (e.g., Damineli et al. 1997, 1998). In this model, flux from η Car B ionizes more completely a portion of the outer wind on the side of η Car B and weakens the hydrogen absorption. For this model to work, our line of sight must intersect the ionized zone.[11] At periastron the flux from η Car B is absorbed/occulted by η Car A and its inner wind, and the H I absorption lines are stronger.

A single star shell ejection model is still invoked by some authors to explain the observed line and continuum variations (e.g., Davidson et al. 2005). Smith et al. (2003) invoked shell ejection to explain the observed variation of the H I P Cygni profiles. In their model, the central source has a fast polar wind that is denser than the equatorial wind. At most phases the equatorial wind is highly ionized and the H I absorption is weak. However, during the spectroscopic event a shell is ejected and the wind becomes symmetric with enhanced H I absorption. The systematic variation of the H I absorption profiles seen in radiation reflected by dust in the Homunculus and the symmetry about the polar axis support this model.

Both models can potentially explain the observed variations of the Weigelt blob spectra. In the single star shell ejection model,

---

[11] By ionized we mean H/H⁺ ∼ 10⁻⁶. In this case the Balmer P Cygni absorption tends to be weak. When H/H⁺ ∼ 10⁻³ or larger, the absorption is strong.

radiation from the central source preferentially escapes in the equatorial regions, ionizing the Weigelt blobs. During the shell ejection, this radiation is blocked, and hence the ionization of the Weigelt blobs decreases. In the binary model, η Car B supplies the harder photons necessary to produce He I, Fe III, etc. When η Car B approaches periastron, η Car A's extended wind, and perhaps η Car A itself, shields the blobs from the ionizing radiation.

Can we distinguish between the single star shell ejection model and the binary model? We interpret the present spectroscopic data as strong support for binarity over a single star shell ejection:

1. The He I emission lines are consistently blueshifted throughout most of the 5.54 yr period. This is not explainable with an axial-symmetric shell ejection, which would give equal amounts of blueshifted and redshifted emission. It is naturally explained by the binary model. In the binary model the He I emission is produced by ionization by the far-UV flux from η Car B followed by recombination. The orbit is highly elliptical, and at apastron (and for most of the orbit) η Car B is in front of η Car A and ionizes the portion of η Car A's wind flowing toward the observer. Therefore, for most of the orbit, the He I is formed in the blueshifted part of η Car A's wind.

2. The double peak profile seen in the He I emission (see Fig. 2) and the velocity variations of these peaks are qualitatively consistent with emission arising from spatially separated regions near a colliding wind interface (Luehrs 1997). The shape and behavior of the He I emission lines in the η Car spectrum are similar to the line variations observed in other colliding wind binaries. The C III λ5698 line is observed to show dramatic line profile variation in the spectra of WR 42, WR 48 (Hill et al. 2000, 2002), and WR 79 (Luehrs 1997; Hill et al. 2000, 2002). C III λ5698 is not present in the η Car spectrum.

3. As noted earlier, a striking characteristic of the He I emission is the dramatic velocity shift across periastron passage. This is similar to radial velocity variations of stars in highly eccentric binary systems and suggests that the emission follows the orbit of one of the stars. In general, it is difficult to see how a single star shell ejection model can explain the complex behavior of the observed He I absorption profiles (see § 6.2.1). Potentially, the velocity jump near $\phi = 1.0$ can be caused by a shell ejection, with the absence of the higher velocity absorption from the previous shell disappearing because of recombination. In a single star shell ejection model, radial velocity variations in absorption would occur since the ejected material accelerates to more negative velocities as it moves away from the star. However, in this model it is hard to explain why the most rapid decrease in velocity occurs close to 2003.5 minimum rather than just after the shell ejection, which would be necessary to provide significant absorption for the entire 5.54 yr cycle. Furthermore, it is not easy to explain why the He I absorption increases in strength from $\phi = 0.80$ in a single star shell ejection model, since this is well before a shell is ejected.

4. While the increase in strength of the H I absorption can be explained by a single star shell ejection model, it is difficult to understand why the He I absorption has its greatest blueshift at $\phi = 1.0$. In most single star shell ejection models, the shell produces low-velocity absorption just after ejection. The observed velocity change occurs across $\phi = 1.0$ and thereafter requires that the shell be ejected at a very high velocity (approximately −600 km s⁻¹) and decelerate just after $\phi = 1.0$ (to approximately −300 km s⁻¹) before reaccelerating. There is no obvious physical explanation for such behavior, other than that the radial velocity variations are caused by orbital motion.
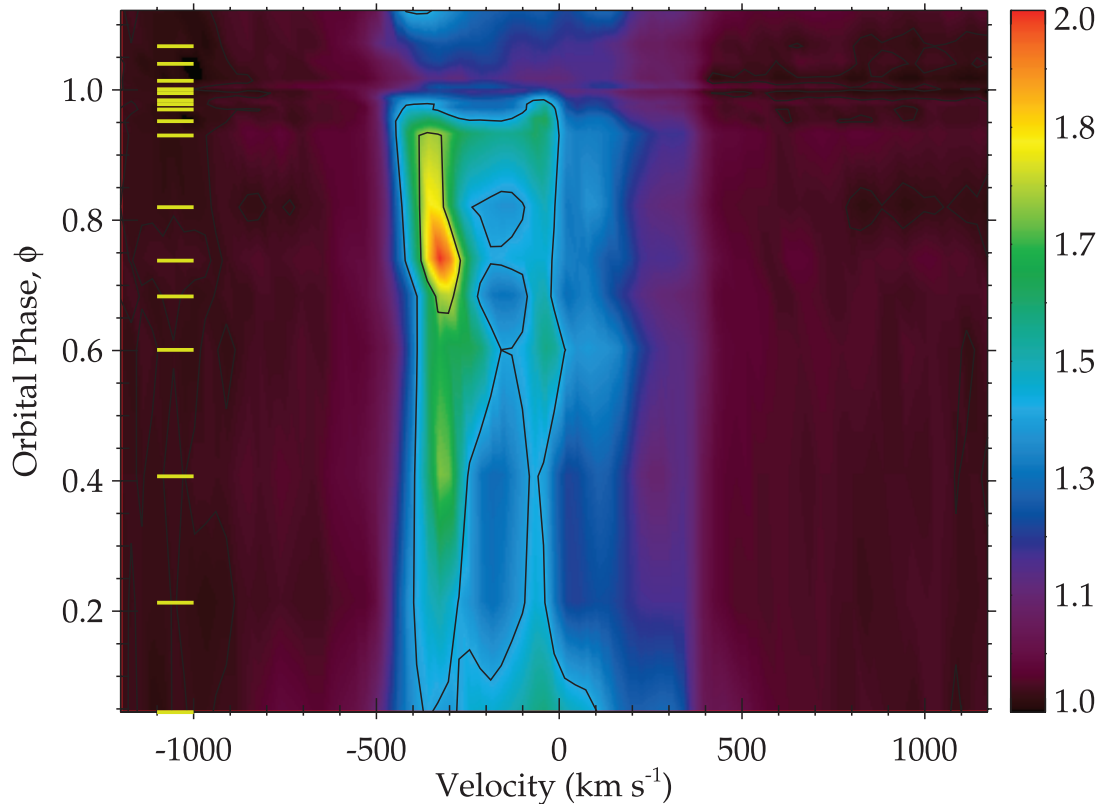
Fig. 14.—Illustration of the [N II] λ5756 variability in intensity and velocity over the spectroscopic period. The contours represent the flux level at -1200 km s^{-1} plus 0.70 and 0.85 of maximum line emission.

5. Another concern is that the H I emission weakens near the time of the shell ejection, before recovering to pre-2003.5 levels, but ejection of a shell should produce more H I emission. In the binary model the weakening can be associated with the disruption of the primary wind by the companion star close to periastron.

6. While high-n members of the Balmer lines show significant variations, P Cygni absorption is present for these lines at all phases, implying that η Car B has a greater influence on the outer wind where, for example, Hα is formed.

7. The variability in Fe II can be naturally explained by a binary model. In the model of Hillier et al. (2006) Fe II emission originates at large radii, extending beyond the binary orbit (30 AU). The companion's far-UV emission will enhance the ionization of nearby outflowing material, weakening both the emission and absorption. Because the orbit is highly elliptical, for most of the orbit η Car B is on the observer's side of η Car A. On the other hand, a single star shell ejection model can explain some of the observed variations if the ejected shell obstructs UV photons from η Car A, lowering the degree of ionization and enhancing the strength of the Fe II P Cygni absorption. However, an axial-symmetric shell ejection usually causes emission variations on both the blue and red sides of the line profile. Only strong variability on the blue side is observed.

There are still uncertainties, and some of the individual points raised above are debatable. However, the consistency between the different line profile diagnostics, the qualitative variation of the observed X-ray fluxes, the variation of the line intensities in the Weigelt blobs, and the location of the Weigelt blobs on the same side of η Car A as η Car B at apastron strongly support the binary scenario. Furthermore, the data suggest that the observed variations are a direct consequence of the variability of the UV radiation and wind of η Car B.

6. INTERPRETATION OF THE VELOCITY VARIABILITY

We have established that line profile variations observed over η Car's spectroscopic cycle are consistent with a binary model. However, a quantitative analysis of the observed variations is difficult because the lower excitation lines are formed in an extended part of the system. An exception is the He I absorption, which presumably is formed in a localized region close to the wind-wind interface. The radial velocity variations in the He I absorption appear to be reminiscent of radial velocity variations from a star in a highly eccentric orbit: a gradual change in radial velocity through most of the cycle, with a rapid shift near periastron passage. We therefore explore what these velocity variations tell us about η Car A, η Car B, and the interacting gas.

We show how the He I absorption line variations can be described by a standard eccentric binary radial velocity curve and demonstrate that the derived value of the eccentricity is consistent with the value derived from the X-ray light curve. To interpret the absorption components and the meaning of the velocity curve, we present a detailed discussion of the colliding wind model and discuss the origin of the He I emission and absorption components.

6.1. The He I Radial Velocity Curve

Line profiles recorded at several phases indicate that the He I absorption is a composite of multiple components. However, only the strongest, least blueshifted feature is traceable over the entire spectroscopic cycle. We created a radial velocity curve for the He I absorption, based on this component. A second high-velocity absorption component appears near the spectroscopic
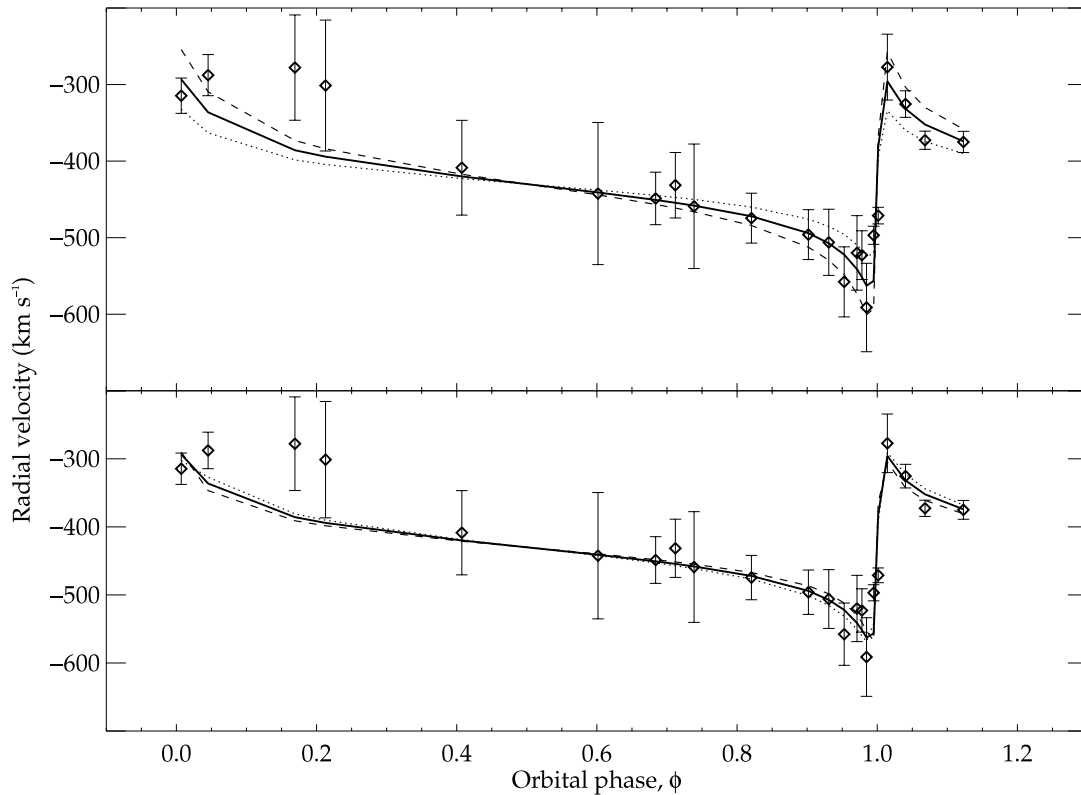
Fig. 15.—Radial velocity as a function of phase derived from the He I absorption. The solid line shows a fit to the data with the parameter given in Table 3 ($K = 140$ km s^{-1}, $e = 0.90$). *Top*: Variation in the velocity amplitude, $K = 100$ km s^{-1} (*dotted line*) and $K = 180$ km s^{-1} (*dashed line*). *Bottom*: Variation of the eccentricity, $e = 0.88$ (*dotted line*) and $e = 0.92$ (*dashed line*). The error bars for the measurements represent an estimated uncertainty of the fit and are proportional to the inverse of measured equivalent width.

minimum (see Fig. 4) and disappears during the recovery phase. Stahl et al. (2005) noted a higher velocity component that appeared near the time of the X-ray low state and claimed it was a result of a shell ejection. Over the brief period in which it was observable it followed a velocity pattern similar to the less blueshifted component, suggesting formation in adjacent regions. We have compared the velocity variation observed in the H I and He I absorption with the radial velocity curve for H I and He I emission derived by Damineli et al. (2000) and with the X-ray light curve (Corcoran 2005). Measured absorption velocities for the He I and H I are presented in Figure 7 along with a plot of the *RXTE* X-ray flux (2–10 keV). The maximum velocity of the He I absorption is about -600 km s^{-1}, which decreased to about -300 km s^{-1} on 2003 June 22, just before the spectroscopic minimum. The striking difference between the velocity variation for the He I and H I wind lines is the drop in velocity after periastron ($\phi = 0.05$), which follows the X-ray drop seen by *Chandra* (Henley 2005). This discontinuity may be a result of absorption in the gas between the primary star and the bow shock, while the H I absorption originates from a volume extended beyond η Car B's orbit. The variation of the He I absorption component is similar to that of a spectroscopic binary. Figure 15 shows the observed He I absorption velocities, along with sample velocity curves for a range of eccentricities and velocity amplitudes. Note that the spectral lines in this analysis have absorption components that are blended with their emission components, making the line profile fitting difficult and decreasing the measurement accuracy. The radial velocity curves for He I, plotted in Figure 15, were calculated using the standard formalism (Aitken 1964):

$$\frac{dz}{dt} = K[e\cos\omega + \cos(\nu + \omega)] + \gamma, \quad (1)$$

where dz/dt is the radial velocity along the line of sight, e is the eccentricity, ω is the longitude of periastron, ν is the true anomaly,[12] and γ is the average velocity. K is

$$K = \frac{2\pi a \sin i}{P\sqrt{1 - e^2}}, \quad (2)$$

where i is the inclination, a is the major axis of the orbit, and P is the spectroscopic period with an assumed beginning at the X-ray low state coinciding with periastron passage. All other parameters are initially free, although we constrain $e > 0.8$ based on the solution of the X-ray light curve (Corcoran et al. 2001). In Figure 15 solutions obtained by varying e and K are plotted. The adopted parameters are given in Table 3.

[12] The relation between the true anomaly, v, and the eccentric anomaly, E, is given by $\tan(v/2) = [(1 + e)/(1 - e)]^{1/2}\tan(E/2)$; E is related to the phase as $2\pi\phi = E - e\sin E$.

TABLE 3
RADIAL VELOCITY CURVE SOLUTION

Parameter	Value
P	2024.0 days[a]
i	41°[b]
γ	-430 km s^{-1}
K	140 km s^{-1}
e	0.9
ω	270°

[a] Corcoran (2005).
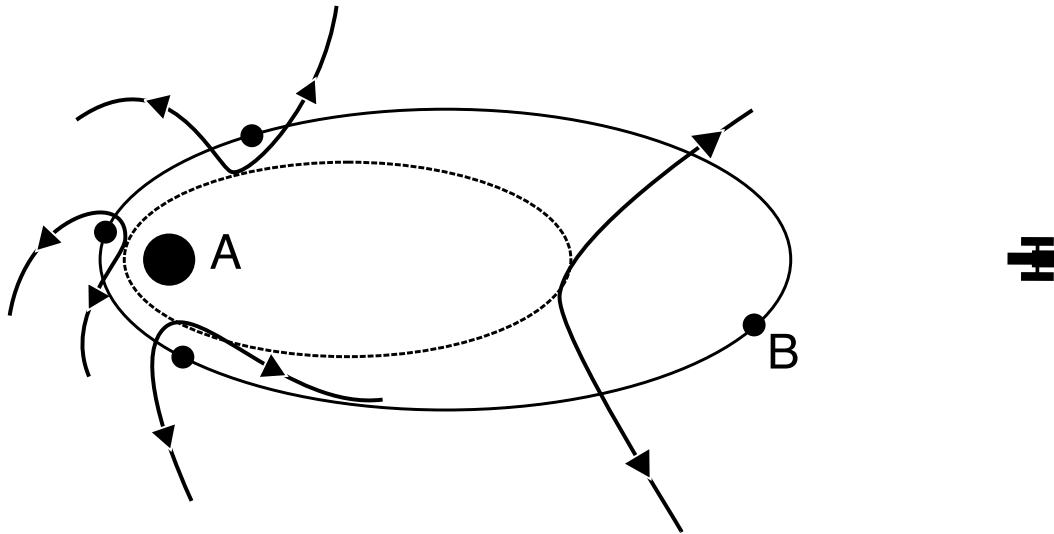[b] Davidson et al. (2001).

Fig. 16.—Cartoon representing the standard view of the colliding wind system in η Car, in which the shock cone is wrapped around η Car B (B). The more massive star η Car A (A) has the slower but denser wind. The arrows show the flow of the gas along the bow shock. The position of *HST* is appropriate for $\omega = 270°$, and the system is likely tilted about $41°$ into the sky plane.

6.2. *Orbital Dynamics*

In most published binary models of the η Car system, η Car A is defined as the primary star and is dominating both the mass and luminosity of the system. Object η Car B is usually assumed to be the hotter, less massive star with a weaker, although much faster, wind. Support for such a scenario comes from the analysis of the X-ray (Henley 2005), far-UV (Iping et al. 2005), and UV/optical (Hillier et al. 2001, 2006) spectra in addition to the modeling of the Weigelt blobs (Verner et al. 2005). Although there is no direct evidence regarding the orbital inclination or the relation of the orbit to the geometry of the Homunculus, the usual assumption is that the inclination of the orbit is the same as for the symmetry axis of the Homunculus and that the orbital plane lies in the intervening disk between the lobes of the Homunculus. Most models (Corcoran et al. 2001; Smith et al. 2004) assume that the longitude of periastron is such that, prior to periastron passage, η Car B is moving away from us and η Car A is moving toward us, as shown in Figure 16. Falceta-Gonçalves et al. (2005) suggested that η Car B is moving toward us just prior to periastron passage. It is more certain that the system has a large eccentricity and that, because of the short duration of the panchromatic variations, periastron passage occurs in the time interval of the X-ray/ionization low state.

The He I P Cygni absorption components are the best localized features in the system since they require high-energy photons and/or collisions to be produced and they arise in outflowing material distributed along the line of sight to the more luminous star. Nevertheless, the interpretation of these features is not straightforward since it is not well understood where the absorbing material is located. The absorber is associated with either the wind of η Car A, the colliding wind interface, the wind of η Car B, or a combination of these. Similarly, the He I emission can arise either in the bow shock or in the portion of the primary wind ionized by η Car B. Downstream absorption in the bow shock has previously been observed in other binary systems such as V444 Cyg (Shore & Brown 1988). However, the thickness of the bow shock in the η Car system and the projection in line of sight provide little absorbing material between η Car A and the observer throughout the orbital period. The ionizing photons of η Car B penetrate deeply into η Car A's wind, creating a substantial He$^+$ zone. In

the following sections we describe the possible location of the absorbing system and discuss implications on the derivation of the system parameters.

6.2.1. *Velocity Variations Caused by Orbital Motion*

The velocity curve shown in Figure 15 is very similar to a radial velocity curve for an object in a highly eccentric orbit. If Figure 15 describes the orbital motion of one of the two objects in the η Car system, then the blueshifted He I absorption over most of the spectroscopic period and the geometry of the system (including the position and variability of the Weigelt blobs) imply that we are tracing absorption in the dense primary wind. The terminal velocity of the absorption profile is consistent with the observed terminal velocity of η Car A and much less than the terminal velocity of η Car B ($\sim$3000 km s^{-1}; Pittard & Corcoran 2003). Wind profiles with a terminal velocity as large as 3000 km s^{-1} are not observed in the η Car spectrum.

The derived radial velocity curve (Fig. 15) confirms the large eccentricity derived from the X-ray light curve (Corcoran et al. 2001) but yields a surprisingly large K-value, $K = 140$ km s^{-1}. This value is inconsistent with the radial velocity amplitude measured in H I, whose origin is associated with η Car A. To determine a mass of both stars in the binary system, radial velocity curves for both objects are needed. However, if only one of the objects is traced, then a mass function describing the relation between the two objects can be created. If the large He I velocity shifts during periastron are solely caused by the orbital motion of one of the stars, then the mass function is

$$f(m_1, m_2) = \frac{K_1^3 P (1 - e^2)^{3/2}}{2\pi G} = \frac{m_2^3 \sin^3 i}{(m_1 + m_2)^2}$$
$$= \frac{m_1 \sin^3 i}{q(q+1)^2} = 50 \, M_\odot,$$

using the values from Table 3, and $q = m_1/m_2$ with the subscripts denoting the observed star (1) and the unseen star (2). With the exception of the possible detection of η Car B in the *FUSE* spectrum (Iping et al. 2005), there is little evidence for spectral features from the companion star. We therefore, initially, associate
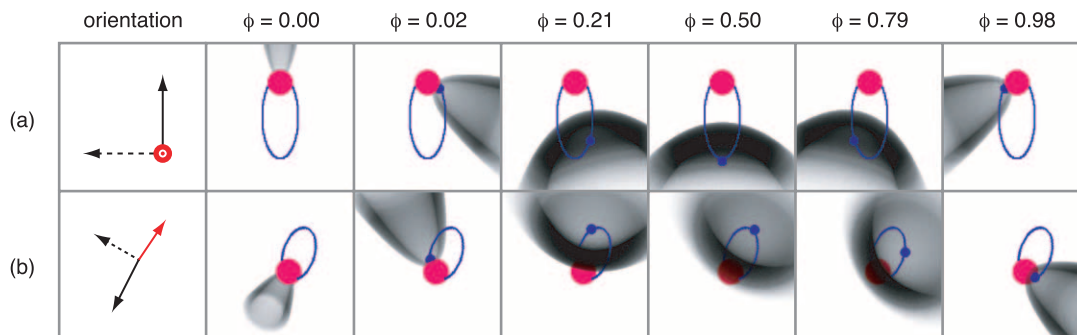
Fig. 17.— Visualization of the He$^+$ zone located in the η Car system. Object η Car A, the larger red stellar component, is shown with a $\sim$9 AU diameter disk, consistent with the apparent 2 μm continuum diameter measured by Weigelt et al. (2007). Object η Car B, the source of the UV radiation, is the smaller blue disk. The gray structure represents the He$^+$ zone, the source of the He I emission and absorption. The top row views the system with the plane lying in the paper: the Z-axis (*red*) points out of the paper, while the X-axis (*dashed arrow*) and the Y-axis lie in the paper. The semimajor axis of η Car B is in the Y-direction and the semiminor axis in the X-direction. The bottom row views the system with the Z-axis (*red*) pointed along the axis of the bipolar Homunculus with Z at $-41°$, rotated about $-45°$ in position angle from north, consistent with the geometry derived by Davidson et al. (2001). Given the locations of the Weigelt blobs plus the orientation of the radio continuum monitored by Duncan & White (2003), the orbit is rotated into the disk plane such that the semimajor axis (Y-direction) projects almost on top of the Z-axis. Note that this visualization does not take into account distortion due to the Coriolis force, which is considerable near periastron ($\phi = 0.00$), but small near apastron ($\phi = 0.50$).

the He I absorption with the primary star. If the observed velocities represent the motion of η Car A, a mass for η Car B for chosen values of η Car A's mass can be derived. This analysis is consistent with a mass of η Car B of 210 $M_\odot$ for a $\sim$20 $M_\odot$ mass of η Car A; i.e., η Car A is the lower mass object in the system with an extreme mass ratio, $q \sim 0.1$. This is the solution with the lowest total mass of the system, but it is only one of many possible solutions with the set of parameters given in Table 3. The orbital plane is assumed to be in the same plane as the intervening disk between the Homunculus, $i = 41°$, but this value is poorly determined. If we use a limiting value of the inclination closer to $90°$, a different set of solutions with a higher mass ratio (0.4–0.6) is obtained; however, η Car B still is the more massive object in the system. This is different than the conventional view of the system in which η Car A has a mass of $\sim$100 $M_\odot$ and is the more massive object.

If the conventional view, as we believe, is correct, it requires that the mass function we derive above is a gross overestimate of the true mass function. This could be due to underestimation of the eccentricity or inclination, or an overestimate of the velocity amplitude, K, or a combination thereof. Note that the argument that the more luminous star is the more massive one assumes the two objects to be unevolved. If this is not the case and, for example, η Car A is on the helium-burning main sequence, then η Car B may be the more massive object in the system.

In the next section we describe how ionization effects, caused by η Car B, may influence the derived value of K.

6.2.2. The Influence of Ionization on the Velocity Amplitude

If the He I absorption is in states populated by recombination in a region of η Car A's wind, which is ionized by η Car B and localized toward η Car A, then the observed absorption-line velocities are a combination of η Car A's wind velocity in the absorbing region and the velocity due to η Car A's orbital motion. Variations in the observed line velocities can be produced by changes either in the orbital velocity of the absorbing gas, in the characteristic outflow velocity of the gas, or a combination thereof.

The location of the ionized region in η Car A's wind is difficult to determine accurately since it depends on the density profile through its distorted wind, combined with the size of the wind-wind collision shock front, which allows more of η Car B's ionizing flux to penetrate into η Car A's wind. We illustrate an undistorted He$^+$ zone for different phases throughout the 5.54 yr

period in Figure 17. We note that even the two-dimensional model of the colliding wind region becomes highly distorted by the Coriolis force near periastron (J. Pittard 2006, private communication). Distortion of the wind-wind interface will greatly affect the derived radial velocity measurements and the derived K-value. Building a detailed three-dimensional model is beyond the scope of this paper. The model shown in Figure 17 simply approximates the wind-wind interface and the He$^+$ boundary as two undistorted parabolical surfaces centered on the line between the two stars.

Figure 17 (*top row*) shows the system as viewed looking down on the orbital plane. We see that, other than near periastron ($\phi = 0$), the He$^+$ structure is predominantly offset from η Car A toward η Car B. In this orientation, the velocity seen in emission will be centered at the system velocity, but the observer would see a range in velocities dependent on the angular curvature of the bow shock in three dimensions. The major part of the H I Lyman radiation escapes down the direction of the major axis and is directed in a small cone along the orbital plane toward the Weigelt blobs.

The bottom row in Figure 17 shows the binary system viewed by the observer, assuming an inclination $i = -41°$, which is appropriate if the orbital plan is in the disk plane between the bipolar lobes of the Homunculus. The orientation depicted in the bottom row of Figure 17 is such that for most of the period, a significant portion of the He$^+$ zone overlaps the line of sight toward η Car A, but at different radial velocities if the wind is accelerating outward from η Car A.

Figure 18 qualitatively shows the effects of ionization on the material in front of the disk of η Car A. The rectangular region represents the material toward η Car A, and the dark gray region represents the He$^+$ zone and scales with the He I column density, proportional to $N(\mathrm{He}^+) \times N(e^-)$. Prior to periastron passage, the companion star mostly ionizes high-velocity wind material far from the primary in the direction of the shock cone, which points away from η Car A. After periastron passage, the shock cone is tilted toward η Car A, so that η Car B mostly ionizes low-velocity material in η Car A's inner wind. X-ray spectra also show a buildup of cool, absorbing material between the colliding winds and the observer for a brief time after periastron passage (Viotti et al. 2002; Corcoran 2005), which blocks ionizing radiation from the companion star from reaching the outer, high-velocity wind material. Thus, after periastron passage the observed velocity
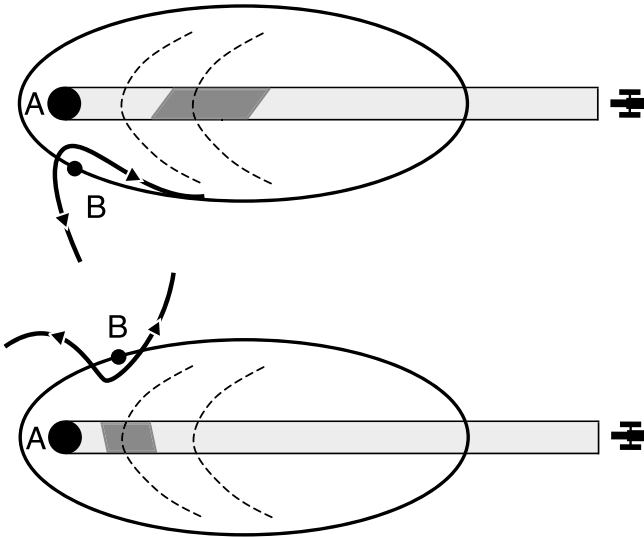
Fig. 18.—Qualitative illustration showing the orbit of η Car B in the reference frame of η Car A and how the ionization of η Car A's wind by η Car B can produce absorption-line velocity variations. The dashed lines represent wind isovelocity contours. The dark gray area represents the section of η Car A's wind, which is ionized by η Car B's flux. Prior to periastron passage (top), η Car B primarily ionizes high-velocity wind material far from η Car A. After periastron passage (bottom), η Car B mostly ionizes low-velocity wind material due to a buildup of cool wind material between the observer and η Car B. This is a qualitative representation and not drawn to scale.

of the absorption system is expected to shift to lower velocities. This means that ionization effects can produce larger velocity variations than would be observed from orbital motion alone, and therefore the velocity amplitude derived in § 6.2.1 does not represent the actual velocity variation due to the orbital motion of η Car A. If the ionized structure was known, the He I radial velocity curve could be corrected for the influence of ionization and the true orbital motion of η Car A could be derived. However, this requires detailed modeling of the dynamics of the wind of η Car A and η Car B.

7. DISCUSSION

Evidence from numerous observations suggests that η Car A is orbited by a hot companion star in a highly eccentric orbit. The velocity curve derived from the He I P Cygni absorption and, to a lesser extent, the variation of H I absorption show periodic behavior very similar to the radial velocity of a star in a highly eccentric orbit with a longitude of periastron $\omega \sim 270°$, which is consistent with the orbital parameters derived from analysis of the *RXTE* X-ray light curve (Corcoran et al. 2001), and also confirm the variation seen in ground-based observation of the Paγ and Paδ emission lines (Damineli et al. 2000). Significant deviations from ω by more than about $10°$ could not describe the observed radial velocity curve. Our solution requires a much larger eccentricity than the solution given by Damineli et al. (2000), $e = 0.9$ instead of $e = 0.65-0.85$. This larger eccentricity helps resolve the discrepancy between the ground-based Paschen line velocities and an earlier report on Paschen line velocities in two observations with *HST* STIS (Davidson et al. 2000). In any event the more complete STIS data set analyzed in this paper clearly shows radial velocity variations of the type expected from orbital motion. Our analysis of the radial velocity curve shows that the orbit is oriented so that the semimajor axis is pointed toward the observer ($\omega = 270°$) but with some orbital inclination (likely $i \sim 41°$) and that η Car A is in front of its companion at peri-

astron. In our simplistic model the He I absorption forms in the wind of η Car A due to ionization by the far-UV flux from η Car B, and the He$^+$ portion of η Car A's wind approaches the observer prior to periastron passage, consistent with the increasing blueshift seen in the He I and H I lines.

One surprising result of our He I absorption analysis is the large derived value of the velocity amplitude, $K = 140$ km s^{-1}. Since the star that is in front at periastron is η Car A, the large K-value, along with the increasingly blueshifted absorption prior to periastron, would imply that η Car A itself is the lower mass object, or, more precisely, that the star whose wind dominates the system is the lower mass object. Such a scenario is not unusual. In most well-studied colliding wind binaries the lower mass star has the stronger wind. A case in point is WR 140, a canonical WC+O colliding wind system, which, like η Car, has a long period ($P = 7.9$ yr), high eccentricity ($e = 0.881 \pm 0.005$; Marchenko et al. 2003), hard X-ray emission, and in which the weaker wind O star dominates the mass and luminosity of the system. An exception to this generalization is the LBV+WR system HD 5980, in which the more massive star is an eruptive variable that currently possesses the stronger wind, although prior to its eruption in 1994 the more massive star had the weaker wind (Koenigsberger 2004).

A more plausible explanation is that the K-value derived from the He I radial velocity curve is overestimated because of ionization effects, as discussed in § 6.2.2. An exact modeling of the effects of η Car B's far-UV flux on the ionization state of η Car A's wind depends sensitively on knowledge of η Car A's wind structure (which is distorted by the wind-wind interaction) and on the companion's far-UV flux, neither of which is well constrained. We qualitatively represent these effects, but our model of an undisturbed primary wind being ionized by the far-UV of the secondary is too simple. Numerous effects may come into play. For example, the wind from η Car A piles up on the colliding wind shock, while radiation and thermal energy from the wind shock may also excite helium. As the system approaches periastron, the evidence is strong that the secondary star approaches to within a few AU of η Car A. When this happens, the winds and atmospheres of the two stars may experience a major disruption. This could have a major influence on the observed line profiles and measured velocities. The Coriolis effect in this very eccentric orbit greatly influences the structure and therefore the derived K-value. It is a matter of controversy whether the colliding wind interface remains intact at this point.

The He I and H I line profiles reveal important information about the binary system. However, only two observations, the first about 1 week before the minimum and the second 1 week afterward, measure the rapid changes in velocity in He I and H I. Much more frequent observations with high spatial resolution are needed. We caution observers that because of nebular scatter of the stellar component and contamination of nebular emission lines, subarcsecond angular resolution is necessary.

8. SUMMARY

We have monitored the He I and H I emission and absorption between 1998.0 and 2004.3. The He I lines generally show blueshifted peculiar profiles, with a dramatic velocity shift across the spectroscopic minimum. These lines are likely produced by the flux of the hot companion star, although energy released in the wind-wind interface region may also play a role. The He I lines show a multicomponent structure, consisting of a broad P Cygni feature with narrow peaks superimposed on top. The lines are generally blueshifted for most of the spectroscopic/orbital cycle, showing that they are produced in the portion of the wind of η Car A that is

flowing toward the observer. We have interpreted the narrow emission line components as formed in spatially separated regions in the bow shock. Hence, the He I lines forming in η Car A's wind in the vicinity of the bow shock are the result of the far-UV flux from the hot η Car B. The H I lines display homogeneous profiles centered at the system velocity and show a smaller shift in velocity across the spectroscopic minimum. The smooth velocity curve for the H I lines implies line formation from a large part of the system.

We have measured the radial velocity and equivalent width variations in the He I absorption and emission lines and created a radial velocity curve from the absorption lines. Using this radial velocity curve, we have calculated a mass function for the binary system and estimated the mass of the hidden companion star and show that either the companion star is the more massive object in the system or our estimate of the velocity amplitude is too large due to ionization effects. We believe that the latter explanation is the more likely one, and that detailed modeling of the radiative

transfer in the system may allow us to constrain the mass function more accurately from the *HST* STIS data.

REFERENCES

Aitken, R. G. 1964, The Binary Stars (New York: Dover)
Corcoran, M. F. 2005, AJ, 129, 2018
Corcoran, M. F., Ishibashi, K., Swank, J. H., & Petre, R. 2001, ApJ, 547, 1034
Damineli, A. 1996, ApJ, 460, L49
Damineli, A., Conti, P. S., & Lopes, D. F. 1997, NewA, 2, 107
Damineli, A., Kaufer, A., Wolf, B., Stahl, O., Lopes, D. F., & de Araújo, F. X. 2000, ApJ, 528, L101
Damineli, A., Stahl, O., Kaufer, A., Wolf, B., Quast, G., & Lopes, D. F. 1998, A&AS, 133, 299
Davidson, K. 1997, NewA, 2, 387
Davidson, K., & Humphreys, R. M. 1997, ARA&A, 35, 1
Davidson, K., Ishibashi, K., Gull, T. R., Humphreys, R. M., & Smith, N. 2000, ApJ, 530, L107
Davidson, K., Smith, N., Gull, T. R., Ishibashi, K., & Hillier, D. J. 2001, AJ, 121, 1569
Davidson, K., et al. 2005, AJ, 129, 900
Duncan, R. A., & White, S. M. 2003, MNRAS, 338, 425
Falceta-Gonçalves, D., Jatenco-Pereira, V., & Abraham, Z. 2005, MNRAS, 357, 895
Feast, M., Whitelock, P., & Marang, F. 2001, MNRAS, 322, 741
Gull, T. R. 2005, in ASP Conf. Ser. 332, The Fate of the Most Massive Stars, ed. R. Humphreys & K. Stanek (San Francisco: ASP), 277
Hamaguchi, K., et al. 2007, ApJ, in press (astro-ph/0702409)
Henley, D. B. 2005, Ph.D. thesis, Univ. Birmingham
Hill, G. M., Moffat, A. F. J., & St-Louis, N. 2002, MNRAS, 335, 1069
Hill, G. M., Moffat, A. F. J., St-Louis, N., & Bartzakos, P. 2000, MNRAS, 318, 402
Hillier, D. J., Crowther, P. A., Najarro, F., & Fullerton, A. W. 1998, A&A, 340, 483
Hillier, D. J., Davidson, K., Ishibashi, K., & Gull, T. 2001, ApJ, 553, 837
Hillier, D. J., et al. 2006, ApJ, 642, 1098
Iping, R. C., Sonneborn, G., Gull, T. R., Massa, D. L., & Hillier, D. J. 2005, ApJ, 633, L37
Ishibashi, K., Corcoran, M. F., Davidson, K., Swank, J. H., Petre, R., Drake, S. A., Damineli, A., & White, S. 1999, ApJ, 524, 983
Koenigsberger, G. 2004, Rev. Mex. AA, 40, 107

Kurucz, R. L. 1988, in Trans. IAU, XXB, ed. M. McNally (Dordrecht: Kluwer), 168
Luehrs, S. 1997, PASP, 109, 504
Marchenko, S. V., et al. 2003, ApJ, 596, 1295
Martin, J. C., Davidson, K., Humphreys, R. M., Hillier, D. J., & Ishibashi, K. 2006, ApJ, 640, 474
Martin, J. C., & Koppelman, M. D. 2004, AJ, 127, 2352
Nielsen, K. E., Ivarsson, S., & Gull, T. R. 2007, ApJS, 168, 289
Osterbrock, D. E., & Ferland, G. J. 2006, Astrophysics of Gaseous Nebulae and Active Galactic Nuclei (2nd. ed.; Sausalito: University Science Books)
Pittard, J. M., & Corcoran, M. F. 2003, in Rev. Mex. AA Conf. Ser., 15, 81
Pollock, A. M. T., Corcoran, M. F., Stevens, I. R., & Williams, P. M. 2005, ApJ, 629, 482
Shore, S. N., & Brown, D. N. 1988, ApJ, 334, 1021
Smith, N. 2004, MNRAS, 351, L15
Smith, N., Davidson, K., Gull, T. R., Ishibashi, K., & Hillier, D. J. 2003, ApJ, 586, 432
Smith, N., Morse, J. A., Collins, N. R., & Gull, T. R. 2004, ApJ, 610, L105
Soker, N. 2005, ApJ, 619, 1064
Stahl, O., Weis, K., Bomans, D. J., Davidson, K., Gull, T. R., & Humphreys, R. M. 2005, A&A, 435, 303
Steiner, J. E., & Damineli, A. 2004, ApJ, 612, L133
van Genderen, A. M., Sterken, C., Allen, W. H., & Liller, W. 2003, A&A, 412, L25
Verner, E., Bruhweiler, F., & Gull, T. 2005, ApJ, 624, 973
Viotti, R. F., et al. 2002, A&A, 385, 874
Weigelt, G., & Ebersberger, J. 1986, A&A, 163, L5
Weigelt, G., et al. 2007, A&A, 464, 87
White, R. L., & Becker, R. H. 1995, ApJ, 451, 352
Whitelock, P. A., Feast, M. W., Marang, F., & Breedt, E. 2004, MNRAS, 352, 447
Williams, P. M., van der Hucht, K. A., Pollock, A. M. T., Florkowski, D. R., van der Woerd, H., & Wamsteker, W. M. 1990, MNRAS, 243, 662
Zanella, R., Wolf, B., & Stahl, O. 1984, A&A, 137, 79
Zethson, T. 2001, Ph.D. thesis, Lund Univ.